FORSCHUNGSZENTRUM JÜLICH GmbH

Institut für Festkörperforschung

A computerized submicron indenter for hardness measurements at variable temperatures

Jiachao Chen Peter Jung

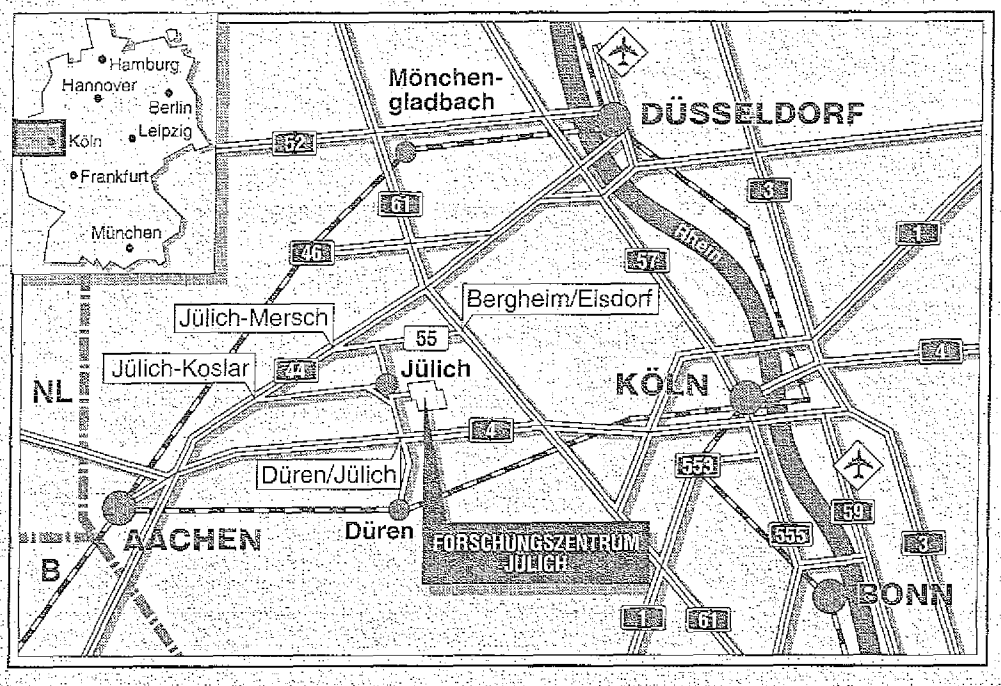

Berichte des Forschungszentrums Jülich ; 2822
ISSN 0944-2952
Institut für Festkörperforschung Jül-2822

Zu beziehen durch: Forschungszentrum Jülich GmbH · Zentralbibliothek
D-52425 Jülich · Bundesrepublik Deutschland
Telefon: 02461/61-6102 · Telefax: 02461/61-6103 · Telex: 833556-70 kfa d

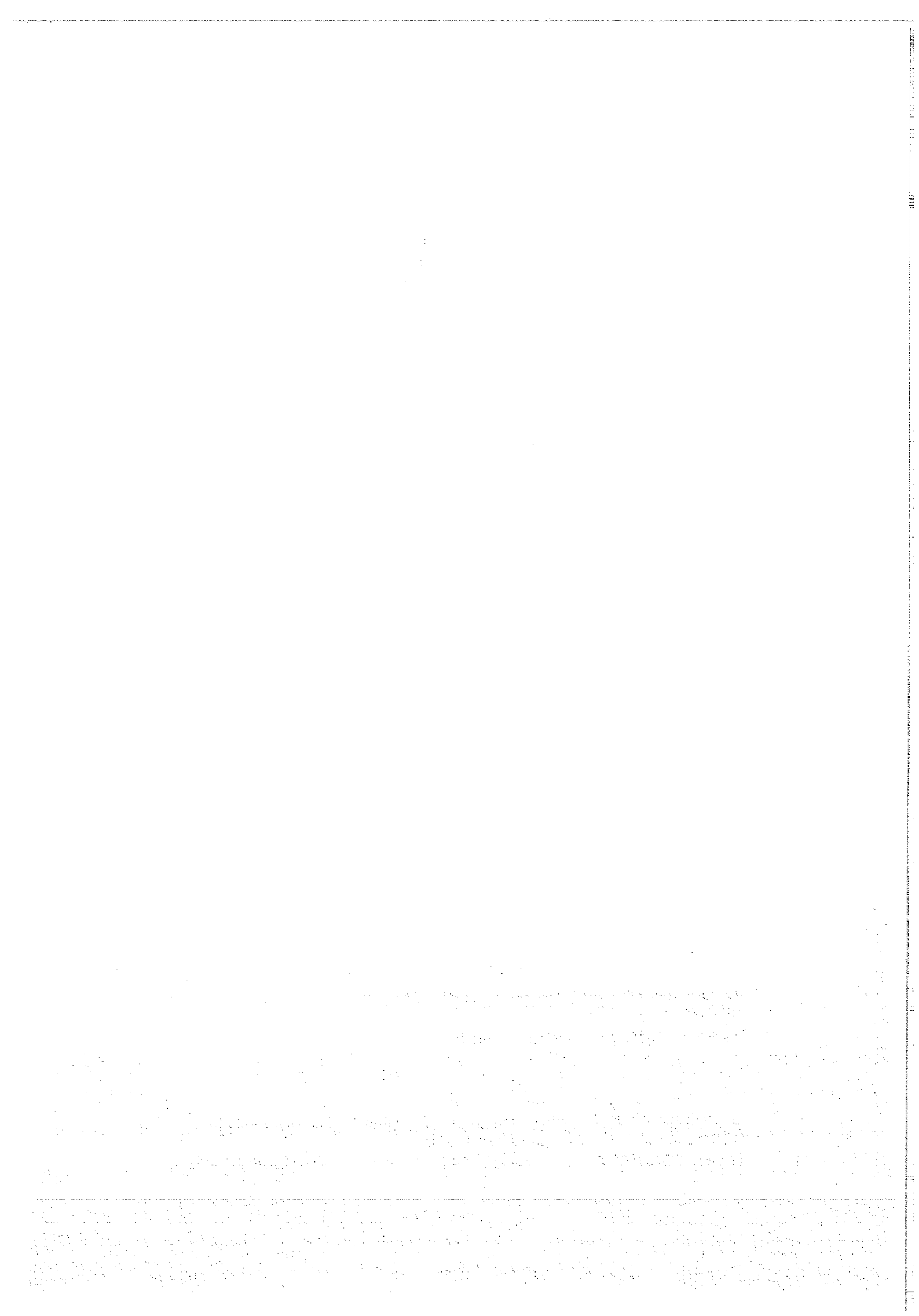

A computerized submicron indenter for hardness measurements at variable temperatures

Jiachao Chen[1)] Peter Jung[2)]

[1)] Inst. Modern Materials, Academia Sinica, Lanzhou, PR China
[2)] Institut für Festkörperforschung, Forschungszentrum Jülich GmbH, D-52425 Jülich

Abstract

A computerized submicron indentation hardness tester which operates at loads from 0.01 to 2 N with 1 mN resolution is described. Penetration proceeds at rates from 20 to 200 nm/s and penetration depth is continuously recorded with a resolution of about 20 nm as a function of load and time. Temperature can be varied from -180° to 400°C with a homogeneity of about 5°C and several exchangeable indenters (Vickers, Berkovich and Knoop) with different angles are available to allow testing with different depth to area ratios. The instrument has been used to investigate indentation size effect (ISE), elastic properties and hardness of thin films on insulators, irradiation effects on braze junctions of austenitic stainless steel and metal-carbon joints, and hardening and embrittlement of martensitic stainless steel by irradiation and helium implantation. Supplementary investigations included hardness measurements under static (creep) and cyclic loading (hardness fatigue) and hardness measurements on stressed specimens.

Ein automatisierter Submicron-Härtetester für Lasten von 0.01 bis 2 N mit 1 mN Auflösung wird vorgestellt. Der Eindruck wird mit einer Absenkgeschwindigkeit von 20 bis 200 nm/s erzeugt wobei die Eindringtiefe laufend als Funktion von Last und Zeit mit einer Auflösung von 20 nm gemessen wird. Temperaturen von -180° bis 400°C können mit einer Homogenität von ca. 5°C eingestellt werden und es steht eine Reihe von austauschbaren Indentern (Vickers, Berkovich und Knoop) mit verschiedenen Winkeln zur Verfügung, welche Messungen mit unterschiedlichen Tiefe-zu-Fläche Verhältnissen ermöglichen. Das Instrument wurde zur Untersuchung des Eindruck-Größen-Effekts (ISE) verwendet, sowie zur Messung der elastischen Eigenschaften und Härte von dünnen Filmen auf Isolatoren, von Bestrahlungseffekten auf Edelstahl- und Metal-Graphit-Lötverbindungen und von Härtung und Versprödung von martensitischem Edelstahl durch Bestrahlung und Heliumimplantation. Ergänzende Untersuchungen umfaßten Härtemessungen unter stationärer (Kriechen) und zyklischer Belastung (Indentations-Ermüdung) und Härtemessungen an Proben unter äußerer Spannung.

Contents page

1. Introduction

The need for techniques to study mechanical properties of surfaces, thin film coatings, layered structures and effects of surface treament, irradiation and implantation has recently rekindled an interest in submicron- and nano-indentation devices for hardness measurements at very low loads. Depth-sensing indentation instruments presently in use [1-4] operate only at room temperature. But as most of the above items include applications below or above ambient temperature, indentation hardness measurements in an extented temperature regime are needed. Therefore a submicron depth-sensing indentation instrument was set up with large flexibility in temperature, indenter shape, load and penetration rate.

While in most mechanical tests a constant volume is deformated by increasing stress and strain, hardness testing imposes virtually constant stress and strain on a steadily increasing volume. A semiempirical analysis [5,6] shows that for cone and pyramid hardness testing the equivalent strain is given by $0.2 \cdot \cot \alpha$, were α is the semiapex angle of the indenter. This means that effective strain in hardness testing can be changed by using indenters of different angles, allowing e.g. determination of work hardening.

Despite extensive hardness testing performed in the past, some pratical problems encountered in microhardness measurements remained unsolved. Two major problems in deriving the hardness of thin layers are:
1) the possible influence of the underlying substrate or matrix
2) the possible dependence of hardness on indentation depth even in homogeneous materials, the so-called indentation size effect (ISE).
In the past ISE was sometimes ascribed to experimental artefacts [7] like defective indenters, cf. also ref.[8], systematic errors in the optical determination of indentation area for small indentations [9], or undefined surface layers from specimen polishing or oxidation [10]. Only recently sufficient experimental evidence for ISE became available at least for some materials [1,11]. But so far it has been studied by different authors in different materials and rather different functional dependences of hardness on indentation size have been obtained. Therefore with the present device ISE was studied systematically in rather different materials with indenters of different angles, giving different effective strain. Included were investigations on the effects of surface preparation and lubrication.

In chapter 2 principles of hardness evaluation in depth sensing experiments are given. The experimental set up is described in chapter 3. Various applications, based on the investigations on ISE (chapter 4) are sketched in chapter 5 and some extending discussions are given in chapter 6.

2. Principles of depth-sensing indentation

Basically hardness has the dimension of stress, i.e. load devided by area. In all standardized hardness tests, area is measured after unloading, i.e. only plastic deformation is considered. For Brinell and Vickers testing, the total "contact" area is used, while for Knoop testing only the area projected on the original surface is taken. In these tests the area is determined by optical measurement of the diagonal lengths of the indentation. For pyramid and Knoop hardness testing $A_p=d_1 \cdot d_2$, where the d_i are the diagonal length of the indentation, the equivalent stress is $H_p/3$, according to a semiempirical analysis [6]. For a Berkovich indenter $A_p=s^2 \cdot \sqrt{3}/4$, where s is the edge length of the triangular indentation. As these standardized tests also dictate other parameters like indenter shape, loading time, maximum load, holding time etc., hardness in this case is not quoted as a physical quantity but as a dimensionless number. In the present study using a variety of indenters and experimental conditions, hardness H_p will uniformly be defined by:

$$H_p = L/A_p \qquad (1)$$

where L is the applied load and A_p is the projected area, i.e. H_p may be considered as the contact stress between indenter and material.

From a depth-sensing instrument, hardness can be obtained without optical imaging of the indentation. The recording of depth during the whole loading and unloading cycle gives additional information on hardness under load and on elastic properties. Depth sensing measurements in addition provide highly improved repeatability and time saving compared to conventional microhardness tests. According to the above definition, the elastic contribution must be subtracted, to obtain hardness. For metals and other elastic-plastic materials, the indentation changes only little during unloading so that in this case the measured hardness is considered also to describe the value under load. This is mainly due to the fact that in these materials the elastic modulus is much larger than the flow stress.

Figure 1 is a schematic representation of the indentation process. For the calculation of hardness, it is neccessary to determine the plastic depth (h_p) which is defined as the depth of the indenter in contact with the specimen under load, while h_t and h_r are maximumum and remaining penetration depth, respectively. From the plastic depth and the indenter geometry, the projected area can then be calculated as will be shown below.

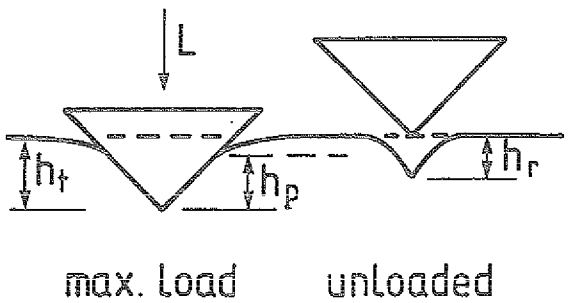

Fig.1: Schematic view of indentation shape during maximum loading and after unloading.

A schematic load-displacement curve is shown in figure 2, where the parts OM and MU are the loading and unloading curve, respectively. Points O and U correspond to the first and last contact with the specimen surface. The maximum penetration h_t is given by OD and the final depth h_r after complete unloading by OU. An ideal loading curve shows a quadratic dependence of L on h [12]. During initial unloading the area in contact with the indenter remains constant [12], which implies a linear unloading curve. Afterwards the contact area between indenter and specimen is reduced continuously with a corresponding deviation of the unloading curve from linearity. Therefore the plastic depth h_p can be approximated by a linear extrapolation of the linear part of the unloading curve [8], giving OC= h_p. i.e. the elastic relaxation is given by h_t-h_p.

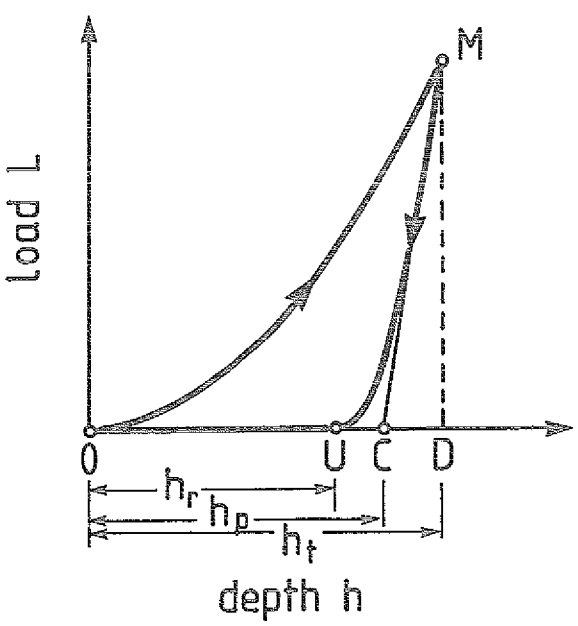

Fig.2: Schematic load versus depth curve, showing loading and unloading behaviour, repectively.

Figure 3a shows a typical indentation curve of aluminum, i.e. load as a function of indentation depth h. The loading is only approximately described by a quadratic dependence of L on h, as will be discussed in chapter 4.1. During unloading all materials initially show a linear relation between L and h which can be extrapolated to the plastic depth hp. The relative amount of elastic relaxation increases with increasing indenter angle and with increasing hardness of the material. The last part of the unloading curve deviates from the linear extrapolation. This deviation from the linear extrapolation also increases with increasing angle α and increasing hardness, giving for silicon at α=80.7° and low load almost complete recovery (fig.3b). This is ascribed to continuous reduction of the contact area between indenter and material, i.e. to a change of shape of the indentation. The remaining angle α' for purely elastic relaxation can be estimated by $tg\alpha' = d/2\sqrt{2}h_r$. Such a change of indentation angle has been observed in ceramic ("hard") materials by optical investigation, with deviations from this relation in ("soft") steels [13].

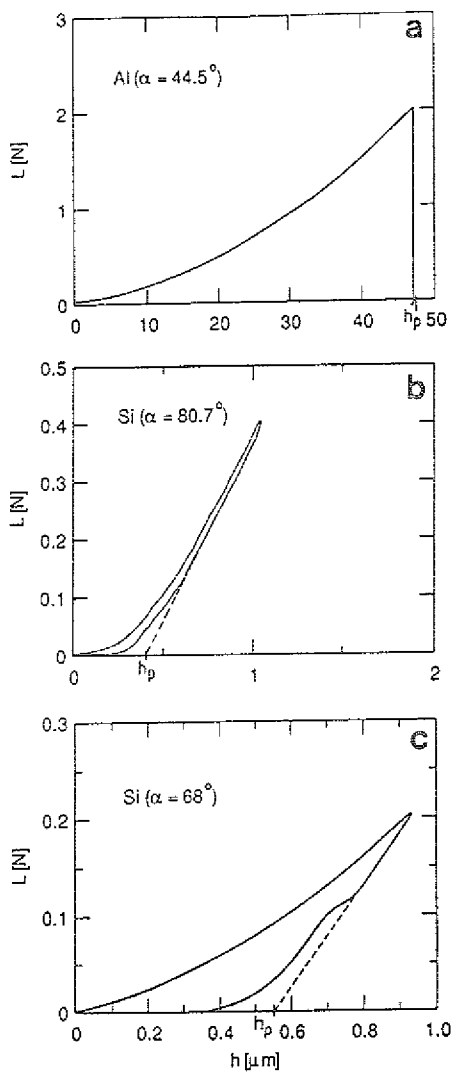

Fig.3: Typical indentation curves for aluminum (a) and silicon (b, c) obtained with indenter angles as indicated.

The strong recovery of silicon causes some ambiguity in the determination of hardness and elastic modulus from indentation measurements. But comparison of h_p with the depth h_d calculated from the diagonals of SEM pictures gave very good agreement also for large indentation angles. This is in contrast to ref.[14] where for a vickers indenter h_d in glass was slighly smaller than h_p. In silicon the deviation from the linear extrapolation does not appear gradually like in the other materials, but rather shows a step-like feature (fig.3c), especially for the sharp indenters. This may be associated with the appearance of cracks which preferentially form at small indentation angles, see figure 4. A special feature appearing mainly with the sharp indenter (α=44.5°) in soft material can be seen in fig.3a. At the end of the unloading curve negative forces up to about 50 mN are observed which may indicate some sticking of the specimen to the indenter due to contraction by elastic recovery.

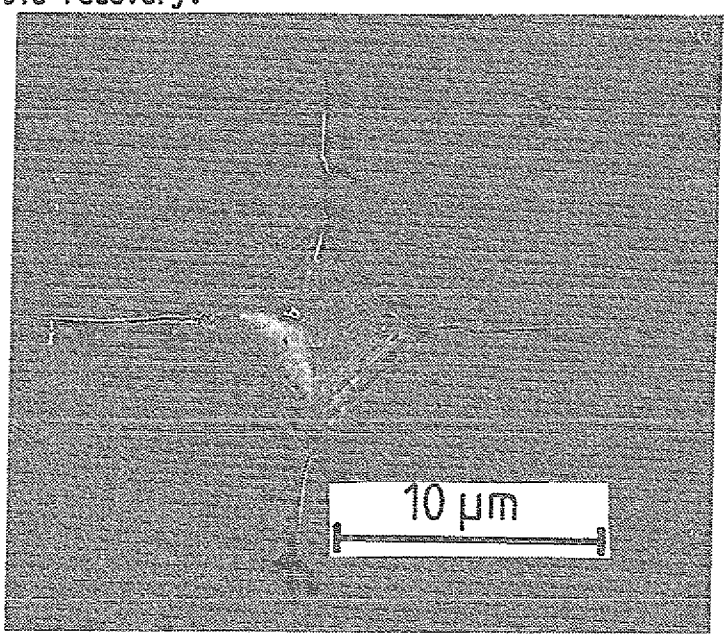

Fig.4: SEM (2.5 kV) picture of α=68° pyramid indentation on silicon causing cracking.

The relation between H_p and plastic depth h_p is given for a square pyramid indenter with semiapex angle α, i.e. angle between indenter planes and stress direction (standard Vickers: α=68°), by:

$$H_p = L \cdot \cot^2\alpha/(4 \cdot h_p^2) \qquad (2a)$$

For a triangular indenter (Berkovich) with angle ß between indenter planes and stress direction by:

$$H_p = L \cdot \cot^2\beta/(3\sqrt{3} \cdot h_p^2) \qquad (2b)$$

For a Knoop indenter with angles α and ß between edges and stress direction (standard: α=86°15′, ß=65°) by:

$$H_p = L \cdot \cot\alpha \cdot \cot\beta/(2 \cdot h_p^2) \qquad (2c)$$

The angle y between indenter planes and stress direction for a Knoop indenter is given by $\cot^2 y = \cot^2\alpha + \cot^2\beta$.

As long as during the initial unloading stage the contact area between indenter and specimen remains constant, unloading can be decribed by an elastic theory derived for a flat punch with a punch base area equal to the projected area of the indentation [12]. From this theory Young's modulus of the specimen can be obtained. The elastic response of a solid after indentation by a cylindrical indenter of radius a is given by [15]:

$$dL/dh=2E'a \tag{3}$$

dL/dh being the slope of the initial linear part of the unloading curve and

$$1/E'=\Sigma[(1-\nu^2)/E] \tag{3a}$$

where E and v are Youngs' Modulus and Poisson's radio, respectively, and the sum includes indenter and specimen material. If the cylindrical indenter is replaced by a square pyramid, i.e. $h_p=d\cdot\cot\alpha/2\sqrt{2}$, of equal projected area ($\pi a^2=d^2/2$) one obtains:

$$E' = (dL/dh)\cdot\sqrt{\pi}\cdot\cot\alpha/(4\cdot h_p) = H_p\cdot\sqrt{\pi}\cdot\mathrm{tg}\alpha/(h_t/h_p-1) \tag{4a}$$

For a Berkovich indenter ($h_p=s\cdot\cot\beta/2\sqrt{3}$, s=edge length of projected area) with $\pi a^2=s^2\cdot\sqrt{3}/4$ the relation becomes:

$$E' =(dL/dh)\cdot\sqrt{\pi}\cdot\cot\beta/(2\cdot 3^{3/4}\cdot h_p) =H_p\cdot\sqrt{\pi}\cdot 3^{3/4}\cdot\mathrm{tg}\beta/(2\cdot(h_t/h_p-1)) \tag{4b}$$

For a Knoop indenter ($h_p=d_\alpha\cdot\cot\alpha/2$, d_α=diagonal length corresponding to angle 2α) with $\pi a^2=d_\alpha\cdot d_\beta/2$ one obtains:

$$E'=(dL/dh)\cdot\sqrt{(\pi\cdot\cot\alpha\cdot\cot\beta)/(2\cdot\sqrt{2}\cdot h_p)}=H_p\cdot\sqrt{(\pi\cdot\mathrm{tg}\alpha\cdot\mathrm{tg}\beta)/(2\cdot(h_t/h_p-1))} \tag{4c}$$

3. Experimental details

3.1 Apparatus

Figure 5 gives a schematic view of the equipment. The specimen holder is mounted on a X-Y stepmotorized table and is surrounded by a furnace which includes an ohmic heater and a cooling pipe for liquid nitrogen. To achieve thermal homogeneity, the specimen holder and the furnace are thermally insultated and shielded. The diamond indenter is mounted on a stainless steel tubing which is moved by a piezo drive and for coarse movements by a vertical (Z) stepping

motor. Step size of the stepping motors is uniformly 0.25 μm, while the piezo drive, which is activated by a linear voltage sweep allows penetration rates from 20 to 200 nm/s. In the load train there is a miniature load cell which measures forces with a resulution of better than 1 mN and an inductive linear displacement transducer (LVDT) for measurement of indenter movement. The relatively large distance between LVDT and indenter, dictated by the need for thermal insulation, caused errors of the measurement of indentation depth by the LVDT due to thermal or elastic strains of the load train. Therefore for precise measurement of penetration depth the capacity between specimen holder and indenter holder was used. Both are electrically insulated and connected to a high precision capacitance bridge (Andeen-Hagerling). The capacity to depth relation is calibrated by LVDT measurement before the indenter gets contact with the specimen. The scatter of the capacity measurements corresponds to a resolution of about 20 nm. Temperature was controlled by the ohmic heater and the cooling pipe. The temperatures of indenter and specimen were measured by thermocouples and differed by less than 5°C. The minimum temperature is about -195°C. But for hardness measurements temperature is limited to about -180°C. Down to this temperature the nitrogen probably evaporates before entering the furnace region, while at lower temperatures evaporation in the furnace causes noticeable vibrations which reduce the resolution. The whole device is mounted in a vacuum recipient, situated on a vibration-isolated table. The system is evacuated by a turbo-molecular pump to pressures below 10^{-3} Pa.

Operation of the device and data aquisition is performed by a personal computer, equipped with an IEEE488 interface which operates the stepping motors, the capacitance bridge, and the piezo drive. In addition it sets the temperature, operates the valves for the liquid nitrogen cooling system and reads the load cell, LVDT and thermocouples via a Philips SYSTEM 21 input-output unit. Figure 6 schematically shows the control circuit. All units can also be operated manually. The load-cell signal is monitored by a limit-switch unit to detect contact with the specimen and to protect the indenter and load cell from overloading (maximum 2.5 N). Temperature is controlled by an analogue PID controller. At temperatures below 100°C, liquid nitrogen is supplied by a 100 l dewar which allows operation for more than 50 hours. Flow rate is controlled by the pressure on the dewar and by an exhaust pump on the down-stream side.

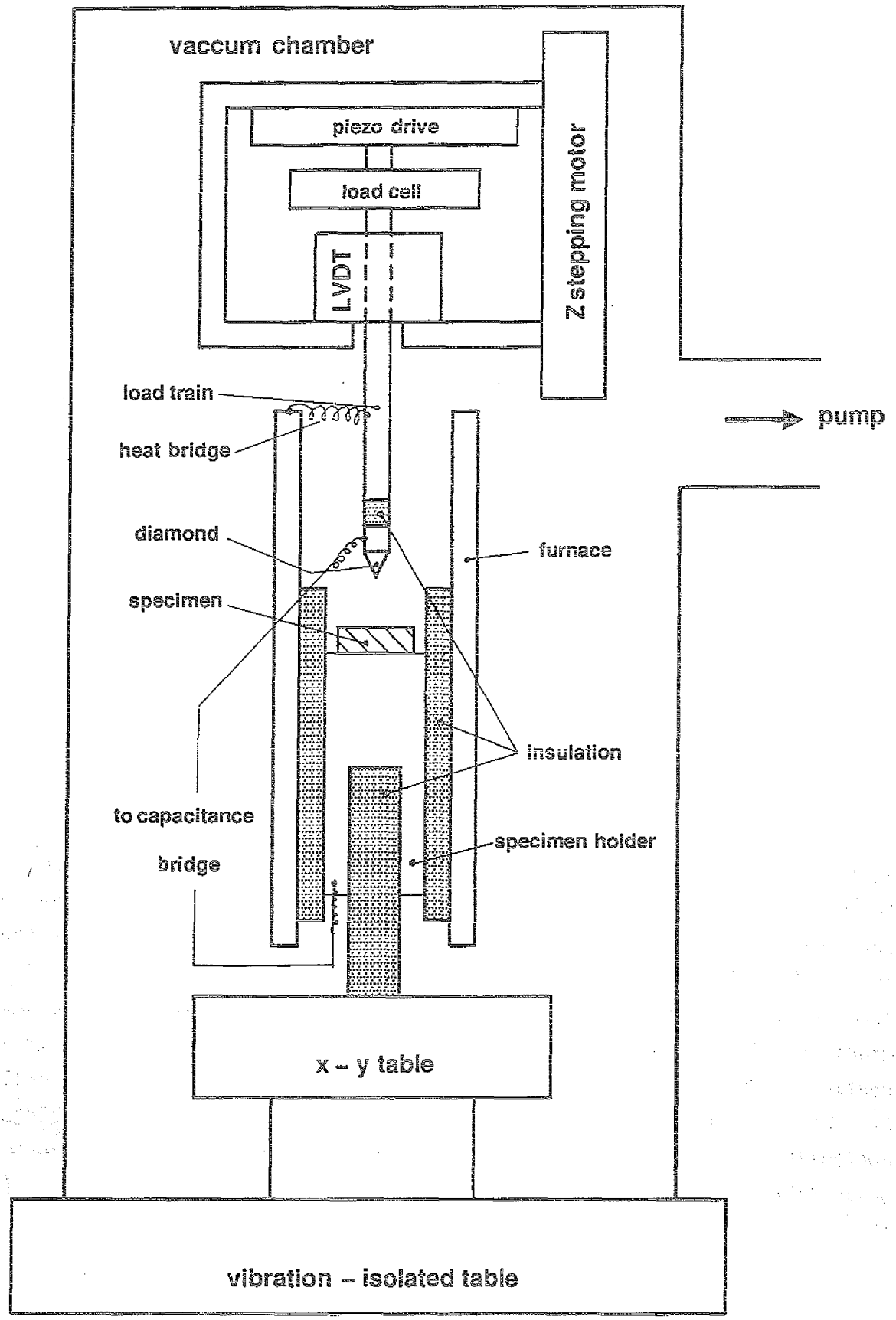

Fig.5: Schematic view of the submicron hardness tester

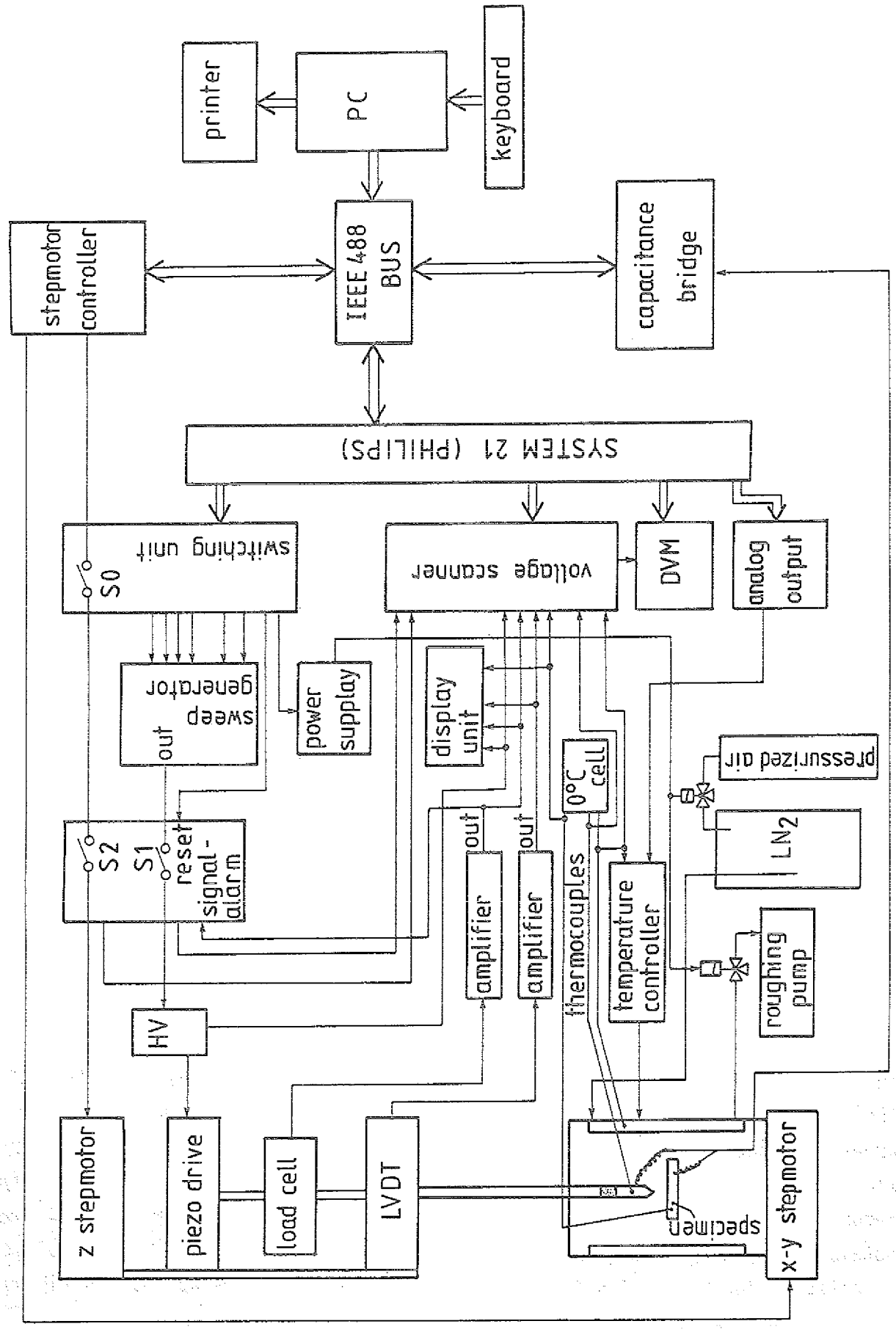

Fig.6. Schematic diagram of operation and data aquisition of the computerized submicron indenter.

In the following a typical indentation cycle is outlined: The indenter is positioned on the specimen relative to a marker with is viewed by a telescope. With some experience this allows positioning within typically 10 μm, which is important for example for investigations of interfaces etc. The program is started by selecting X-Y positions on the specimen and the corresponding temperatures (from -180°C to 400°C) or alternatively loads (from .005 to 2 N). The layout of the indentations can lateron be used for identification when investigations by SEM including chemical analysis by EDX are desired. Then the position of the surface of the specimen is sensed by moving the indenter by the Z-drive. Subsequently the indentation at the preselected positions and temperatures are performed, with forces, displacements, temperatures and time being recorded by the computer. After each temperature change a waiting time of about 1 hour is added to allow for temperature equilibrium. During changing of the X-Y positions the indenter is elevated by about 100 μm to avoid contact with surface roughnesses. Coarse Z-movements are performed by the Z-stepping motor, while only the last 40 μm above the surface are done by the piezo drive. The indenter can also be kept on one position with constant load for a preselected holding time (indentation creep) or can be repeatedly applied to the same position (indentation fatigue). All data are saved on disk and evaluated by seperate programs.

3.2 Diamond indenter

A variety of pyramid diamond indenters were prepared for the present instrument, including square pyramid indenters with semiapex angles α of 45°, 68° (standard Vickers) and 81°, triangular Berkovich indenters with surface-to-normal angles ß of 41°, 65° and 79° (having the same depth to area ratios as the above pyramid indenters), and standard Knoop indenters (α=86°15′, ß=65°). The indenter angles agree within 0.1° as checked by optical goniometry, see table I.

The shape of the indenters is critical for precise hardness measurements [1,8]. Therefore a series of indentations of loads from 0.01 to 1 N were produced on annealed and electropolished stainless steel for imaging in a scanning eletron microscope (SEM, Hitachi S-4100) under normal incidence (fig. 7). For larger indentations, when optical imaging became possible, good agreement with SEM was obtained. A comparison of projected area as determined by SEM and plastic indentation depth h_p gives the exact shape of the indenters as show in figure 8 for pyramid indenters by plotting average diagonal length versus h_p. The solid lines correspond to the semiapex angles derived from optical goniometry. The

offset h_0 of this lines from h_p=0 indicates some blunting of the indenter's tips. h_0 values of square-pyramid and triangular indenters are included in table I. Instead of h_0 a blunting radius r_0 can be fitted which is defined by:

$$r_0 = h_0 \cdot \sin\alpha/(1-\sin\alpha) \qquad (5)$$

In the following, hardness values are always given after correction for indenter bluntness, i.e. the given hardness values always correspond to $2L/d^2$.

Table I: Summary of angles α, bluntness h_0 and length l_0 of a possible ridge on the indenter tip (see figure 7) of quadratic pyramid (V) and triangular pyramid (B) indenter. V136° and B65° correspond to standard Vickers and Berkovich indenters, respectively.

indenter	V90°/2	V136°/1	V136°/2	V163°	B41°	B65°/2	B79°
α	88.2°	136°	136°	161.4°	40.7°	64.7°	81.5°
h_0(µm)	0.22	0.14	0.08	0.05	0.4	≈0	≈0
l_0(µm)	0.5	≈0	≈0	≈0	-	-	-

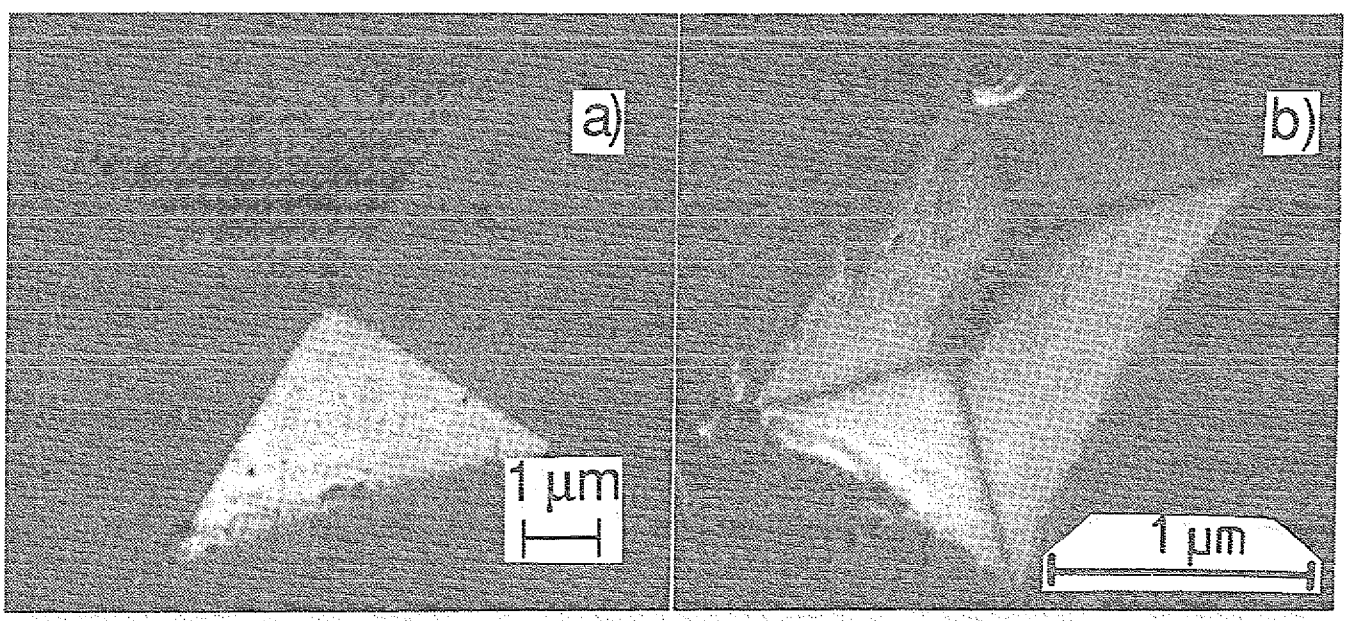

Fig.7: Typical SEM (2.5 kV) images of indentations on annealed austenitic stainless steel with an almost perfect pyramid indenter (a) and with an indenter having a ridge of about 0.5 µm (b).

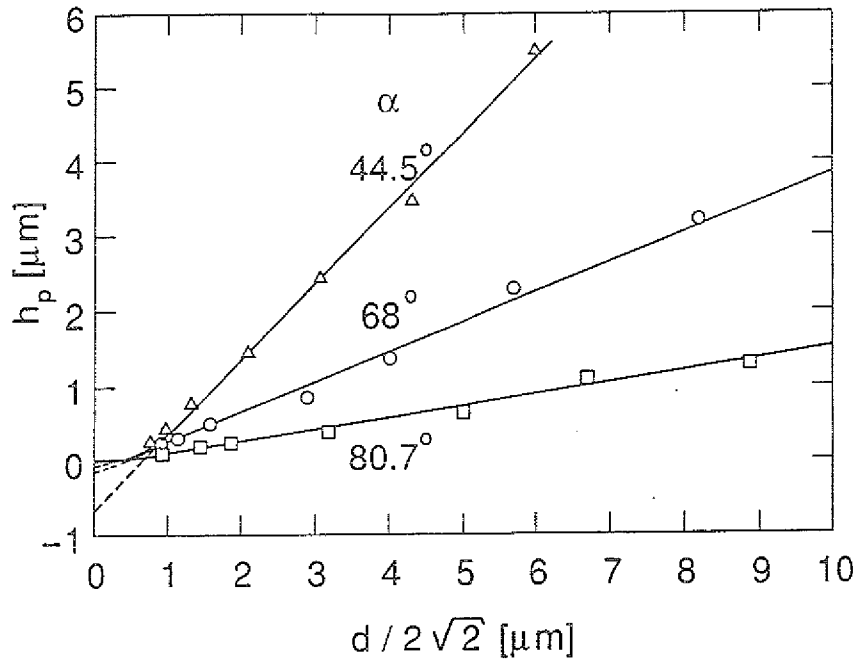

Fig.8: Relation between indentation depth h_p and half edge length (=d/2√2) from SEM of pyramid indentation in 316L. The solid lines indicate the optically determined semi-apex angles α of 44.5°, 68° and 80.7°. The offset of this line on the ordinate indicates effective bluntnesses of the indenters by about 0.65, 0.14 and ≤0.05 µm, respectively.

3.3 Specimen mounting

The inner diameter of the furnace allows specimen sizes up to 10 mm diameter. As a general rule the indentation diagonal should be less than 1/3 of specimen thickness to obtain correct hardness values [16], i.e. for a Vickers indenter the maximum depth must be less than 1/20 of the thickness. This limit is set by the demand that the deformed volume does not reach the backside surface of the specimen. This limit is only sufficient if the specimen is well supported by the holder, i.e. no elastic bending due to the load occurs. If specimens are very thin or if the support area is not perfectly flat, especially measurements of Young's modulus can be significantly influenced by bending. This problem may be somewhat reduced by the present capacitive depth measurement relative to the specimen surface. Nevertheless all foil specimen were glued to the specimen holder by a two-component epoxi (UHU PLUS) which gave best results for temperatures up to 150°C. For measurements at higher temperature several ceramic glues were tested but did not give fully satisfying results as bubbles of ≈100 µm diamenter formed during hardening, see figure 9. Figure 10 shows measurements of Young's modulus for different foil thicknesses using the epoxi. The figure shows that Young's modulus becomes independent on thickness when the foil is thicker than 100 µm for loads of 1 N and below.

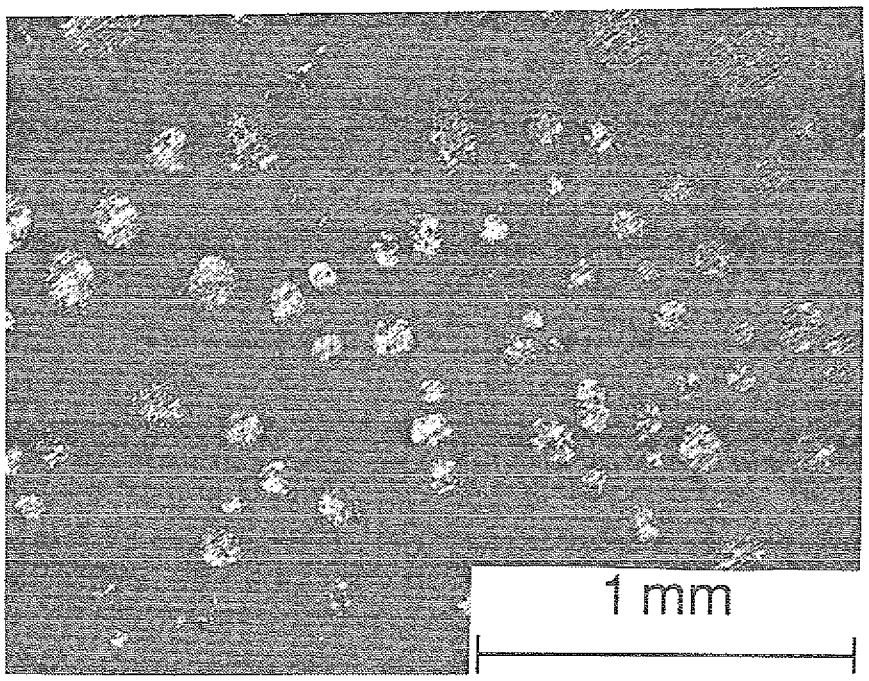

Fig.9: Optical micrograph of ceramic glue after removing of the specimen, showing bubbles which formed during mounting and hardening.

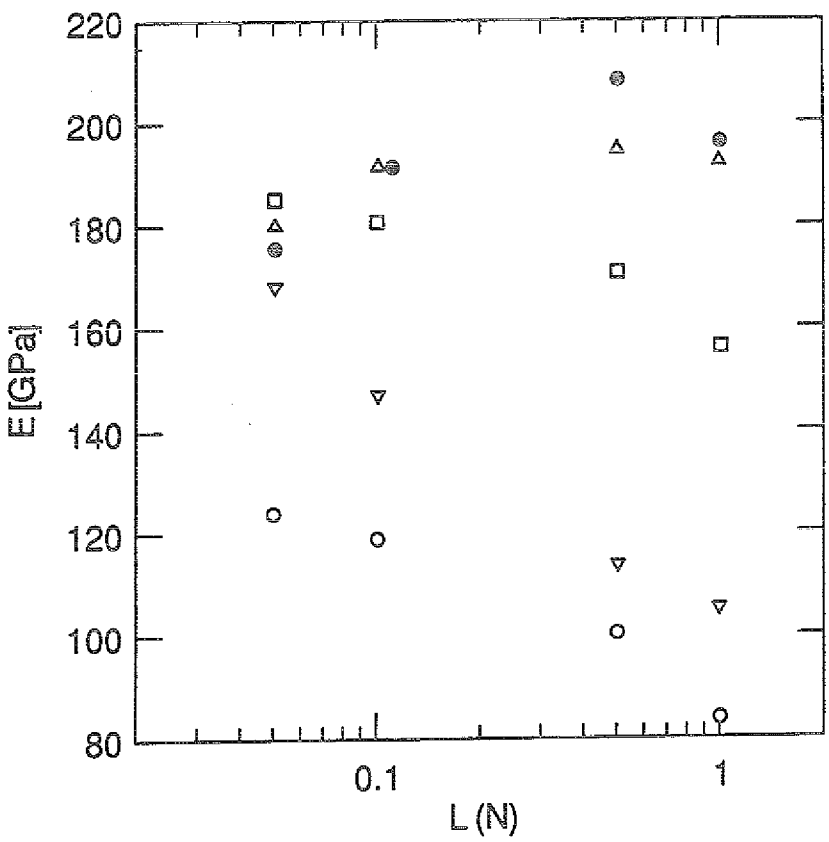

Fig.10: Young's modulus of austenitic 316L stainless steel as a function of load L for specimen thicknesses of 25 µm (○), 50 µm (▽), 100 µm (□), 200 µm (△) and bulk material (●).

3.4 Surface preparation

Standard surface preparation of the specimen was polishing with diamond paste of 1 or 0.25 μm grain size. The parameters and pretreatment of specimen used to investigate ISE are given in table II. Some of the aluminum and copper specimens were eletropolished. For details see table III. It was found that aluminum (fig.11) was the only material which showed a significant effect of surface treatment, namely a higher hardness for polishing with 1 μm grain compared to 0.25 μm and electropolishing. In an attempt to investigate the effect of friction between the indenter and the specimen on hardness measurement, some electropolished Cu and Si specimen were also tested immersed in silicon oil. Within experimental error this did not affect hardness in contrast to results in ref.[17] where a significant indentation size effect at small depth disappeared by lubrication.

Table II: Specimen parameters and pretreatment

Material	purity [%]	thickness [μm]	annealing	surface preparation [a]
aluminum	99.995	500	0.5h:500°C	d/1, d/0.25, ep
copper	99.9996	500	0.5h:700°C	d/1, d/0.25, ep
316L	[b]	100	0.5h:1050°C	d/1, ep
DIN1.4914	[c]	100	0.5h:1075°C+2h:T[c]	d/1
tungsten	99.95	100	as received[d]	d/1
silicon	[e]	280	as received	d/1

[a] d/x=polished with diamond paste of grain size x[μm]; ep=electropolishing
[b] The stainless steel 316L has the main constituents [wt%]: 65Fe-17.6Cr-12.3Ni-2.3Mo-1.8Mn-0.5Si-0.2Cu-0.03P-0.024C) and is the austenitic reference materials in the European fusion programme.
[c] The stainless steel DIN1.4914 (MANET I, MANET II in parathesis) has the main constituents [wt%]: 86.0(86.3)Fe-10.7(10.3)Cr-0.85(0.67)Ni-0.79(0.78)Mn-0.75(0.57)Mo-0.4(0.19)Si-0.22(0.2)V-0.13(0.10)C-0.034(0.024)N and is the martensitic reference materials in the European fusion programme. Stress relief temperature T=700°C (I) and 750°C (II).
[d] Johnson-Matthey GmbH, Germany
[e] Reinstsilizium from Wacker Chemitronic, Germany

Table III: Electropolishing conditions

Material	eletrolyte	cathode	voltage(V)	temperature(°C)
Cu	50% H_2O, 50% H_3PO^4	Cu	1.8-2	RT
Al	100 ml HNO_3, 100 ml CH_3OH, 4 ml HCl	Al	5	RT

4. Analysis of indentation size effect

4.1. Hardness

For the investigation of ISE, the quadratic diamond pyramid indenters with semiapex angles α of 44.5°, 68.0°(Vickers) and 80.7° were used and loads from 0.01 N to 2 N were applied. Indentation hardness was measured at room temperature on high purity aluminum and copper, representing soft materials, high purity silicon and tungsten, representing hard materials and on austenitic 316L and martensitic DIN 1.4914 stainless steel, representing alloys of intermediate hardness. In figs.11 to 14 mean stresses $2L/d^2$, i.e. load divided by projected indentation area are plotted as a function of the reciprocal average diagonal length 1/d for Al, Cu, 316L, DIN1.4914, Si and W, respectively. As already mentioned, aluminum was the only material which showed a significant effect of surface treatment. Included in fig.11 are Vickers data from ref.[18] which are considerably above the present results, possibly indicating lower purity or less effective annealing. In figure 12 the Cu-data from ref.[18] are also higher, while data from ref.[19] are in very good agreement with the present results. In copper and the harder material no remarkable effect of specimen surface preparation was observed, also immersion in silicon oil had no marked effect, cf. also fig.14, in contrast to refs.[17,20]. The harder steel (DIN 1.4914) in figure 13 shows ISE only for the sharp indenter (α=44.5°) while the two other indenters give no load dependence of hardness. ISE is also not observed in tungsten and silicon (fig. 14). The 80.7° indenter gives for tungsten even a slight reduction of stress with decreasing depth, i.e. some kind of inverse ISE. The same is observed for silicon with the 68° and 44.5° indenters, while the 80.7° data of silicon show too much scatter already at rather high loads. At low loads the extrapolated depth from the 80.7° indenter in silicon approaches almost zero and no hardness data could be derived, cf. fig.9b. In Si also no ISE was observed in refs.[1,8] when the indenters were corrected for geometrical deficiencies. The hardness values for Si from ref.[8] match the present values exactly, while those from ref.[1] are considerably lower. Especially for silicon indentation at higher loads (i.e. smaller 1/d) caused cracking (see fig.7) and therefore are not included in the figure.

The dependence of H_p on d^{-1} in fig.11 to 13 indicates indentation size effects in Al, Cu, and in the steels. For large loads a linear increase is observed which can be described by:

$$H_p = H_\infty + U/d \qquad (6)$$

while eventually constant values H_0 are reached for small loads i.e. large d^{-1} values. The intercept H_∞ on the ordinate gives the mean stress at large indentation and is related to the conventional definition of microhardness DPH by:

$$DPH = H_\infty \cdot \sin\alpha \qquad (7)$$

Often the transition from a higher hardness at small loads to a lower hardness at higher loads is tentatively ascribed to the existence of a harder surface layer. Depending on which law of superposition of hardness contributions from surface layer and substrate is used, dependences of hardness on indentation depth are obtained which qualitatively approach the results in figs.11-13 [21,22]. But a more quantitative comparison to the calculations in ref.[21] shows that the constant hardness at low depth is reached around a ratio $2 \cdot t/d \approx 1$ to 2, where t is the thickness of the surface layer. As the present data show this transition around $1/d \approx 0.07$ to 0.15 μm^{-1}, layer thickness around 7 μm would result, similar for all materials. Layers of such thickness, either of compositional (oxides) or mechanical (hardening) origin, certainly do not exist on the present specimens. Also the insensitivity of ISE to surface preparation strongly suggests that a surface layer is not the cause of ISE, with the possible exception of Al. An alternative explanation of the linear 1/d relation in figures 11 to 13 is that ISE is caused by an additional hardness contributions δH at the perimeter of the indentation as suggested in ref.[18]. The mean stress H_p may then tentatively be described by a superposition of the hardness in the centre (H_∞) and in an area along the rim (H_0):

$$H_p = H_\infty + f \cdot (H_0 - H_\infty) \qquad \text{for } H_p < H_0 \qquad (8)$$

If a constant width w of the rim area around the indentation of diagonal d is assumed, the area fraction f of the rim area is given by :

$$f = 4\sqrt{2} \cdot w \cdot (1 - \sqrt{2} \cdot w/d)/d \qquad \text{for } w < d/2\sqrt{2} \qquad (9)$$

A rim of constant width would e.g. not suit to a pile-up region, which rather would give w proportional to d. A comparison of equations (8) and (9) yields:

$$w \approx U/4\sqrt{2} \cdot (H_0 - H_\infty) \qquad (10)$$

Fits of equation (8) to the data in figs.11-13 with the parameters H_∞, H_0 and w (see table IV) are given by the solid lines. H_0/H_∞ and w show no systematic

dependence on indenter shape and material, but attain values of 1 to 2.6 and 1 to 3 μm, respectively.

Table IV: Poisson's ratios v, parameters H_∞, H_0/H_∞ and w used in the fits in figures 11 to 13, extrapolated 2% yield strengths $H_\infty/3$ and strain hardening coefficients m from fig.15. The three values given for H_∞, H_0/H_∞ and w correspond to semi-apex angles α=44.5°, 68° and 80.7°, respectively.

Material	v	H_∞ [MPa]	H_0/H_∞	w [μm]	$H_\infty(2\%)/3$ [MPa]	m
aluminum	0.33	206/182/136	2.3/2.4/2.6	2.0/1.4/1.0	39	0.30
copper	0.36	581/380/240	1.7/1.8/2.1	2.4/3.1/3.0	63	0.49
316L	0.26	1565/1220/882	1.6/1.7/1.5	1.3/1.5/2.5	190	0.31
DIN1.4914	0.28	2195/2590/2480	1.4/1.0/1.0	3.0/ - / -	830	<0
tungsten	0.45	8900/8650/7800	1.	-	2600	0.07
silicon	0.28	15500/17700/17700	1.	-	5900	0.

Recent investigations on Vickers hardness of copper [19] also showed some levelling-off of hardness around $1/d \approx 0.2$ μm^{-1} (see fig.12) but at even lower loads again an increase of hardness was observed. On the other hand these results of ref.[19] at very low loads must be taken with some caution as obviously the indenter was not calibrated by TEM or SEM as in refs.[1,8] or in the present work. For example disregarding of the bluntness of the present Vickers indenter would produce an error of about 30% for an indentation depth of $\leq$1 μm. Even the more perfect Berkovitch indenter in refs.[1,8] would give an error of $\geq$ 10%.

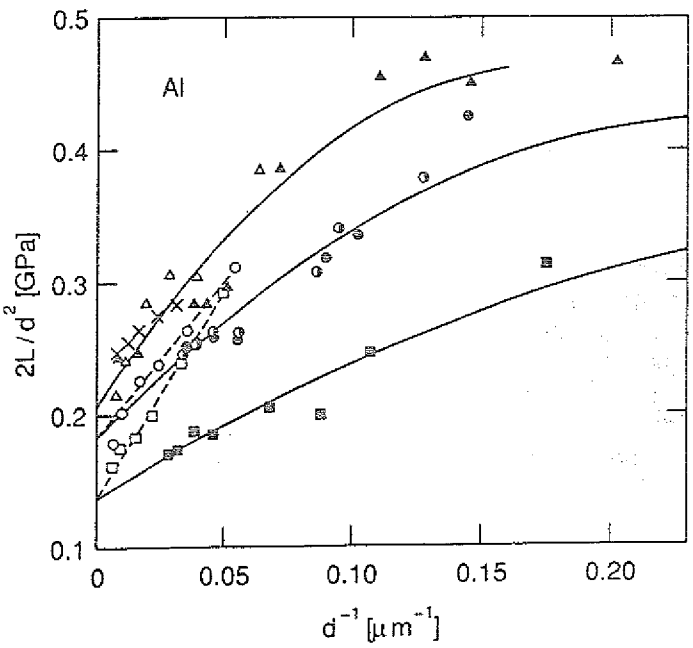

Fig.11: Mean stress $2L/d^2$ as a function of reciprocal mean diagonal length d^{-1} in aluminum for indentation angles α of 44.5° (△, ▲), 68° (○,●,◉) and 80.7° (□, ▣), respectively. Empty, full and half-filled symbols indicate diamond polishing with 1, 1/4μm grain size and electropolishing, respectively. Included are the results from ref. [18] (×) for a Vickers indenter (α=68°).

The behaviour of silicon and tungsten (fig.14), i.e. some decrease of hardness with decreasing load is qualitatively different from the ISE of the other materials. As already mentioned the results on these hard materials may be subject to some error due to the small remaining indentation depth h_p and as furthermore the linear extrapolation (fig.3c) may not adequately describe the elastic recovery in these material causing some uncertainty in the determination of h_p at very low indentation depth .

Aside from a purely phenomenological descriptions of ISE [23], several explanations for a higher hardness at the rim of the indentation have been proposed. The higher hardness was ascribed to inhomogeneous deformation in this area [18], to enhanced deformation of a thin surface layer at the rim [24], and to hardness contribution from pile-up [25]. As already mentioned the independence of w on depth d rules out the pile-up model. The supposition of a surface layer [24] implies that the surface layer contributes to ISE only along the rim, while actually also contributions from the inner part of the indentation should be expected. But this would result in a different dependence on d. Additionally the insensitivity to surface preparation stands against this conjecture. Therefore mainly the independence of ISE on surface preparation and the virtually constant value of w suggest that ISE is an inherent property of materials with not too high hardness and may result from a change of dislocation behaviour due to geometrical constraints [10,11,26].

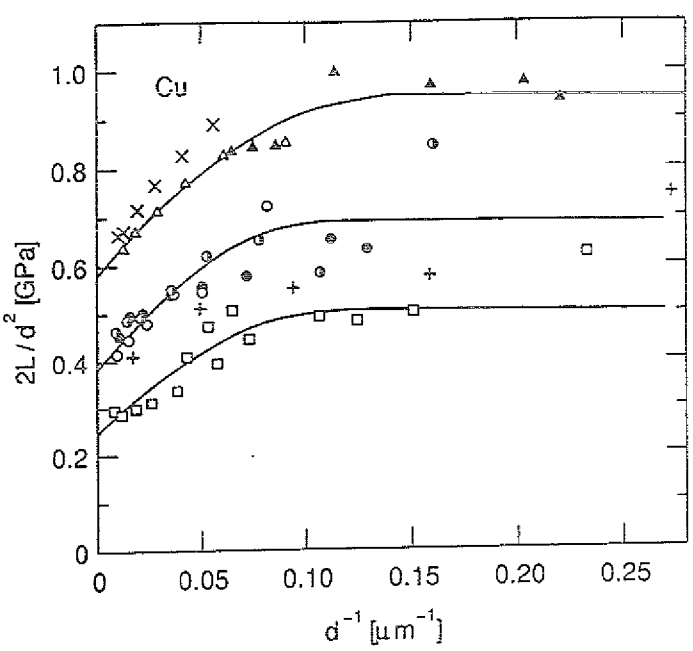

Fig.12: Mean stress $2L/d^2$ as a function of reciprocal mean diagonal length d^{-1} in copper, 1μm diamond polished, for indentation angles α of 44.5° (△, ▲), 68° (○,●,⊕) and 80.7° (□), respectively. For comparison data are included which were obtained by the indenter shown in fig.7b (▲), from electropolished specimens (⊕) and from electropolished specimens immersed in silicon oil (⊕). Included are the results for Vickers indenters (α=68°) from ref.[18] (x) and from ref.[19] (+).

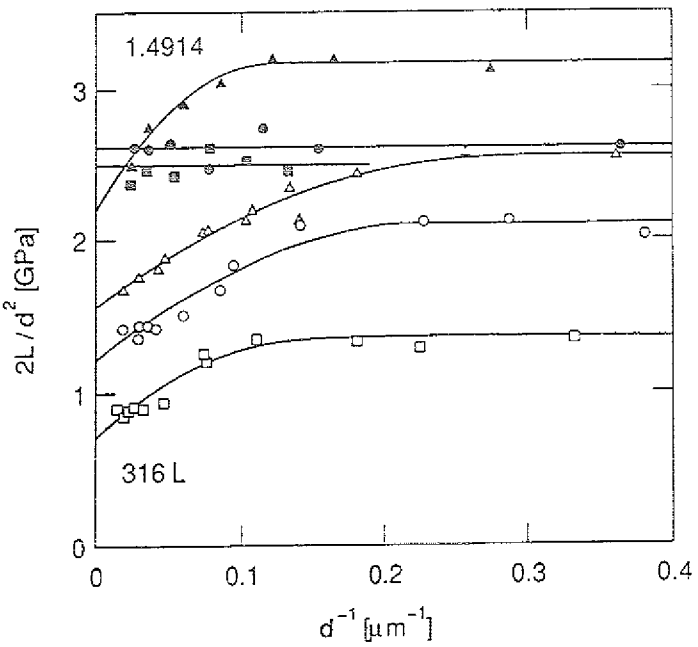

Fig.13: Mean stress $2L/d^2$ as a function of reciprocal mean diagonal length d^{-1} of AISI 316L (open symbols) and DIN 1.4914 (full) for indentation angles α of 44.5° (△, ▲), 68° (o, ●) and 80.7° (□, ■), respectively. For 316L two different 44.5° indenters gave identical results.

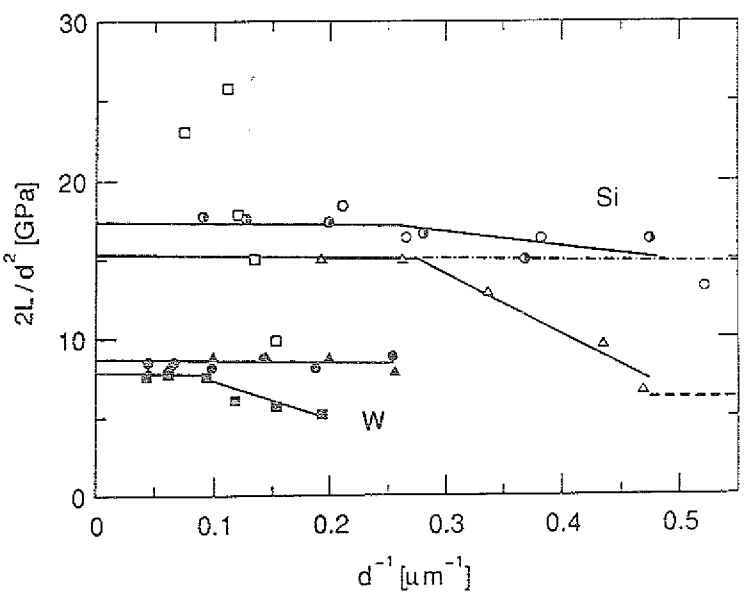

Fig.14: Mean stress $2L/d^2$ as a function of reciprocal mean diagonal length d^{-1} of tungsten (full) and silicon (open symbols) for indentation angles α of 44.5° (△, ▲), 68° (o, ●) and 80.7° (□, ■), respectively. The half-filled symbols indicate Si immersed in silicon-oil. Included are results from ref.[8] (-•-) and ref.[1] (--) for silicon obtained with triangular Berkovich indenters which simulate the d/h ratio of a Vicker's indenter.

4.2. Work hardening

In figure 15 effective stresses $H_\infty/3$ are plotted over the effective strains $\epsilon=0.2\cdot\cot\alpha$ [9]. The log/log plot in figure 15 allows to derive strain hardening coefficients m, defined by:

$$m = \log \sigma \,/\, \log \epsilon \qquad (11)$$

and to extrapolate yield strengths. To avoid too large uncertainties from wide extrapolation only the 2% yield strength is given in table IV together with strain hardening coefficients. These $H_\infty(2\%)/3$ values compare reasonably to $\sigma_{0.2}$ yield strength values in Cu (50 MPa [27]), 316L (250 MPa [28]) and DIN1.4914 (620 MPa [29]). While the softer materials Al, Cu and 316L show significant strain hardening, the martensitic steel shows a reduction of strength at higher strains in agreement with tensile tests [30] where this behaviour was ascribed to softening caused by replacement of the original martensitic lath structur by a softer dislocation cell structure during straining. The brittle materials W and especially Si practically show no effect of strain but a constant value H_∞. This fact indicates that hardness related to the projected area of the indentation is a more adequate material parameter than DPH which is related to the contact area, cf. equation (7), as DPH of Si and W would decrease with increasing strain.

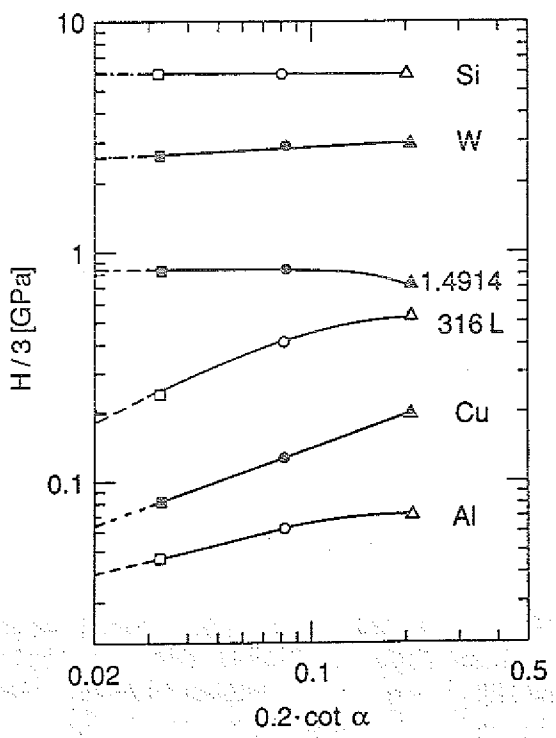

Fig.15: Estimated flow stress $H_\infty/3$ as a function of effective strain, given by $0.2\cdot\cot\alpha$ for materials as indicated.

4.3. Young's modulus

From the unloading curves, information on the elastic properties can be obtained as given by equations (4) and (3a). Values of Young's modulus E derived from the unloading curves according to equations (4) are shown in figure 16 as a function of load. The v values used are given in table IV and for the diamond indenters $E/(1-v^2)=10^{12}$ [Pa] was used. The E values show no significant dependence on indenter shape and only Al, Si and W show some dependence of E on load. For Si and W the remarks on hardness determination at low loads apply also for E, i.e. possibly some systematic error at very small h_p. In general the E-values are in good agreement with literature [31] as included in figure 16.

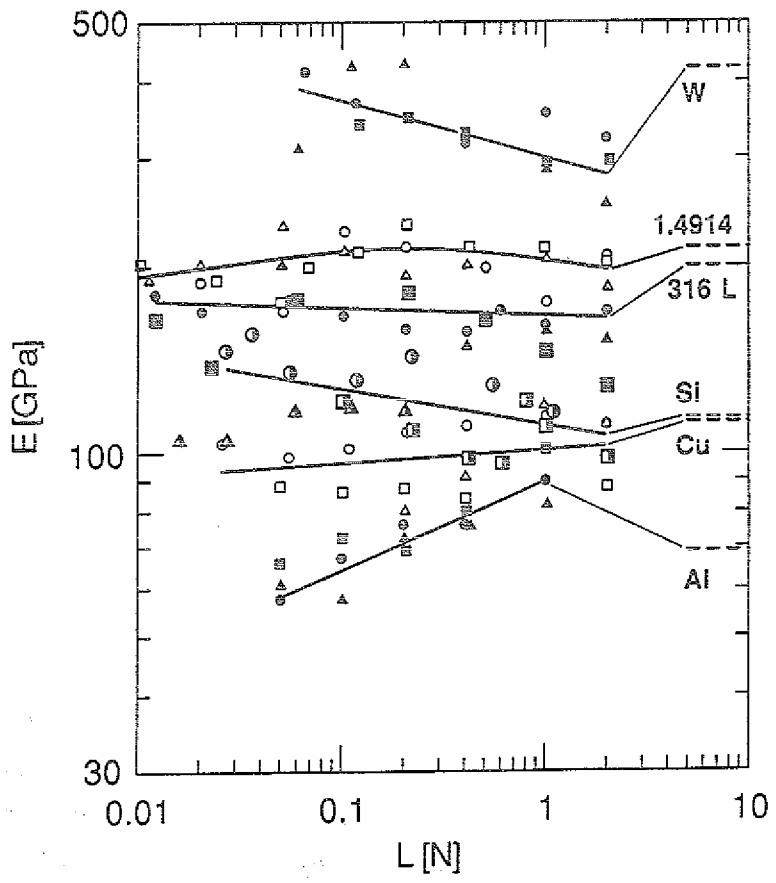

Fig.16: Young's modulus E derived from the unloading curves acçording to equation (3) as a function of load L for indenter angles α of 44.5°, 68° and 80.7°, for Al (▲,●,■), Cu (△,o,□), Si (⧋,⊙,▣), 316L (▲,●,■), DIN 1.4914 (△,o,□) and W (▲,●,■). Included are E modulus data from literature (-- [31].

5. Applications of submicron hardness testing

5.1. Effect of irradiation and of helium implantation on the hardness of martensitic stainless steel

Martensitic stainless steels have been proposed for first wall and structural material of future fusion reactors on account of their superior resistance to void swelling and helium embrittlement. On the other hand, irradiation induced increase of the ductile-to-brittle-transition-temperature (DBTT) is one of the major concerns with respect to the use of these materials in irradiation environments [32]. The standard technique for DBTT measurement is fracturing of Charpy-V-notched (CVN) specimens. Even CVN tests using so-called subsize specimens [31-36] involve specimen volumes ≥200 mm^3 and thicknesses ≥3 mm. As specimen thickness is limited to much smaller values in irradiation or implantation experiments employing ion beams and as only small irradiation volumes will be available in high energy neutron sources [37], other techniques are explored for DBTT evaluation under irradiation, using miniaturized CVN [38], disc compact tension [39,40], and miniaturized tensile specimens [41-43]. Specimen size is reduced to thin TEM disks of 3 mm diameter in disk bend, i.e. ball punch or shear punch tests [44-47], while microhardness tests even allow a large number of measurements on one TEM disk. One major problem is to correlate irradiation induced changes observed by these techniques to changes in the standard CVN test. Up to now it was found that the miniaturized CVN- [33,34,48] and disk bend tests [46,49] on martensitic or ferritic steels give clear transitions in the temperature dependence of absorbed energy but at lower temperatures compared to standard CVN. In the disk bend tests this shift can be reduced by using notched specimens and/or sharper punches [50]. On the other hand tensile tests give no clear temperature step which could be assigned to DBTT [51,52]. But even if a property such as tensile strength does not show a clear transition in the DBTT temperature regime, this does not exclude that irradiation induced changes of this property can be correlated to a shift of DBTT, e.g. refs.[53-55].

It is assumed [33,56] that brittle fracture occurs, when the flow stress reaches the stress for cleavage fracture. As the dependence of cleavage stress on temperature [57] and probably also on irradiation dose is weak, the shift of DBTT by irradiation is primarily determined by an increase of flow stress. Previous studies have shown that irradiation induced changes in tensile strength and also shifts of DBTT are correlated to changes of microhardness at room temperature [54]. For correlation of microhardness and disk bend tests see refs.[59,60]. Also in ceramics hardness correlates very well with fracture

toughness (for a compilation of suggested relations see refs.[61,62]). The effect of helium on DBTT of ferritic/ martensitic steels has not been investigated so far, as helium production in these materials by transmutation in fast reactors is only possible by strongly increased nickel content, which unavoidibly influences the mechanical properties [63]. On the other hand helium implantation limits the specimen thickness to the range of the α-particles, e.g. $\approx$100 μm for 28 MeV α in steels, which is far below the value accessible to CVN tests. Inspite of being the technique which by far needs the smallest sample size, the temperature dependence of microhardness of ferritic/martensitic steels has not been investigated up to now. Therefore the present study investigated effects of irradiation and/or helium implantation on the temperature dependence of microhardness of these materials and possible correlations to DBTT.

The MANET version of DIN 1.4914 is the ferritic/martensitic reference material in the European fusion programm. In the present study it was used in the MANET I and mostly MANET II specifications. Composition and heat treatments of MANET I and II are given in table II. The 100 μm thick foil specimens, polished by 1 μm diamond paste and soldered with indium to a water cooled copper heat sink, were implanted with α particles. Details of the implantation apparatus are given elsewhere [64]. Homogeneous implantation of helium was achieved by degrading the particle's energy by a rotating wheel with aluminum foils of different thickness on its circumference. Specimens were implanted to helium concentrations of 7.9, 36 and 185 atppm, at implantation rates of about 0.02 atppm/s. According to ref.[65] the helium implantation was accompanied by the production of displacement damage of $5.4 \cdot 10^{-4}$, $2.5 \cdot 10^{-3}$ and $1.3 \cdot 10^{-2}$ dpa, respectively, at a rate of $1.4 \cdot 10^{-6}$ dpa/s. In an attempt to separate effects of helium and of displacement damage, some specimens were also irradiated without degrader, i.e. the α-particles passed through the specimens producing displacement damage without implantation. These specimens received displacement doses of $9.6 \cdot 10^{-4}$, $1.3 \cdot 10^{-2}$ and $1.1 \cdot 10^{-1}$ dpa at a rate of $3.5 \cdot 10^{-6}$ dpa/s. The specimen temperature remained below 100°C during irradiation and below 170°C during unsoldering.

Microhardness measurements were performed on these specimens also after annealing for 2 hours at 450°C and 650°C, respectively. To compare the effect of annealing to damage production at elevated temperatures, specimens were also investigated which were proton irradiated at 520°C or He-implanted at 650°C. These specimens were cooled by flowing purified helium gas and temperature was controlled by pyrometry and resistance measurement.

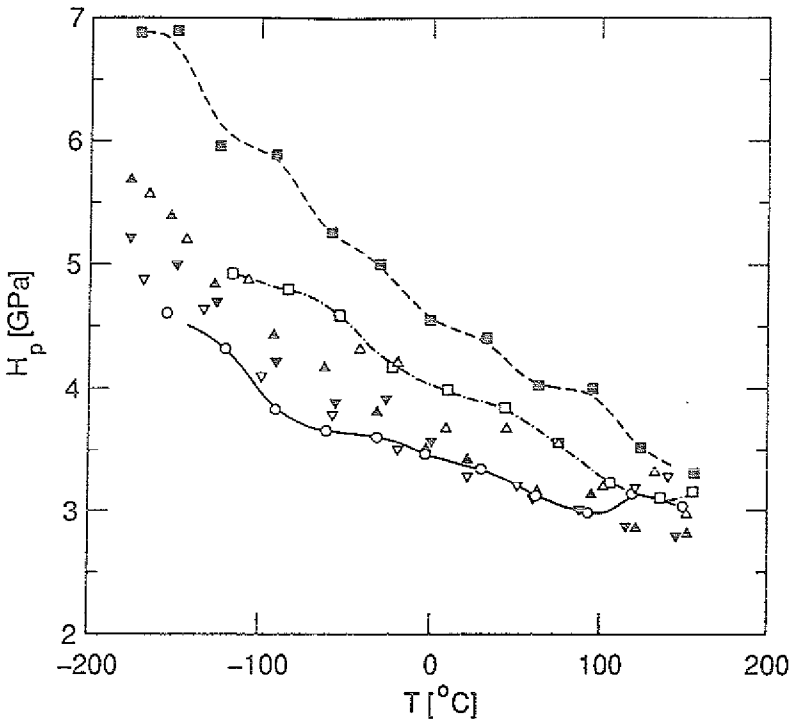

Fig.17: Microhardness versus temperature of specimens unirradiated (o) and irradiated to displacement doses of $9.6 \cdot 10^{-4}$ (▽), $1.3 \cdot 10^{-2}$ (△) and $1.1 \cdot 10^{-1}$ (▣) dpa. Included are specimens which were homogeneously implanted with helium to atomic concentrations of 7.9 (▽), 36 (△) and 185 (□) atppm, corresponding to displacement doses of $5.4 \cdot 10^{-4}$, $2.5 \cdot 10^{-3}$ and $1.3 \cdot 10^{-2}$, respectively.

The measurements of microhardness and Young's modulus were performed with quadratic pyramid diamond indenters with semiapex angles of 44.1° and 68.0°(Vickers), respectively, with a maximum load of 1 N at temperatures from -160° to 150°C. At each temperature the average of five indentations was taken. Figure 17 shows microhardness as a function of temperature of unirradiated MANET II and of specimens irradiated or implanted to various doses. The temperature dependence of the unirradiated material is in fair agreement with measurements of the yield stress [66-68] of pure iron, if $\sigma_Y = H_p/3$ is assumed. The hardness measurements show no change by intermittent heating to 160°C. Irradiation as well as helium implantation increase hardness or alternatively speaking, shift the hardness (i.e flow stress) curves to higher temperatures. This shift only slightly diminishes at the higher temperatures. Most of the curves show two more or less clearly resolved steps with an intermediate plateau at hardness values between 3.5 and 4.0 GPa. The DBTT of unirradiated MANET of about -25°C [36] corresponds on the hardness curve in fig.17 to ≈3.57 GPa. In figure 18 the temperature at which H_p=3.57 GPa is reached, is plotted for the irradiated and implanted specimens as a function of displacement dose. Temperature shifts up to almost 200°C are obtained with significantly larger values for the implanted specimens compared to the irradiated ones at equal displacement dose.

Annealing behaviour of those specimens irradiated, respectively implanted to the highest doses are shown in figure 19. Most of the irradiation induced increase of hardness of the He-implanted as well as of the irradiated specimen recovers already by annealing to 450°C. After the 450°C annealing the 185 atppm He specimen retains a temperature shift of 40°C, while the $1.1 \cdot 10^{-1}$ dpa specimen retains a shift of ≈25°C only below the plateau temperature. Annealing at 650°C brings also the He-implanted specimen back to the original hardness values.

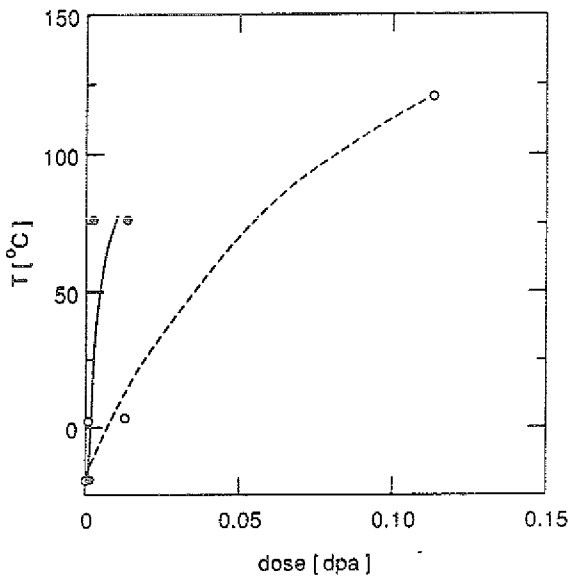

Fig.18: Temperature at hardness H_p=3.57 GPa as a function of displacement dose for irradiated (o,--) and He-implanted specimens (●,-).

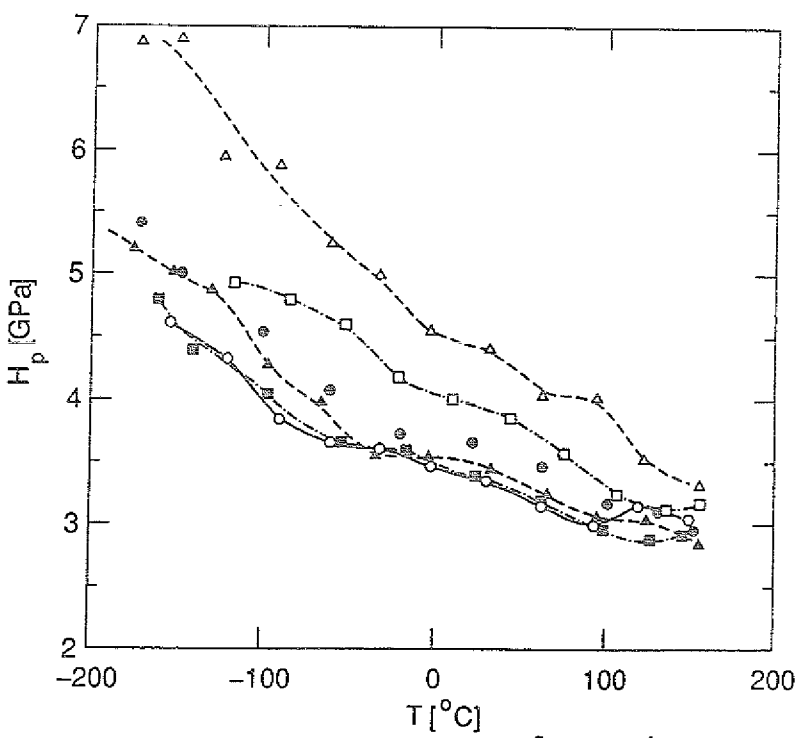

Fig.19: Microhardness versus temperature of specimens, unirradiated (o), irradiated to a displacement dose of $1.1 \cdot 10^{-1}$ (△) dpa, and implanted with 185 atppm He (□). The irradiated specimen was annealed at 450°C (▲) and the implanted specimen at 450° (●) and 650°C (■), respectively.

For hardness measurements after irradiation or implantation at elevated temperatures MANET I specimens from previous experiments were available. These results are therefore not fully comparable to the above results on MANET II. In figure 20 hardness measurements are given on a specimen irradiated with 6.2 MeV protons at 520°C to a displacement dose of 0.55 dpa [69] and on specimens implanted at 600°C to helium concentrations of 33 and ≈ 1000 atppm, respectively [70]. For comparison hardness measurements at room temperature were also taken from the unirradiated end pieces of the specimens (crosses). These values were in good mutual agreement and matched about the value of the 33 atppm curve. Even the 1000 atppm data show significant deviation only at temperatures above -60°C. This is in contrast to the results after annealing in figure 19, where after 450°C a small excess hardness was retained uniformly over the whole temperature regime which then completely disappeared after annealing at 650°C. On the other hand the proton irradiated specimen shows higher hardness at temperatures from -120 to +100°C. This is again in contrast to figure 19 where the 450°C annealing left some hardening only at temperatures below -40°C. These results indicate a significant difference in the behaviour of specimens which were irradiated or implanted at elevated temperatures and those which were annealed after irradiation or implantation at room temperature.

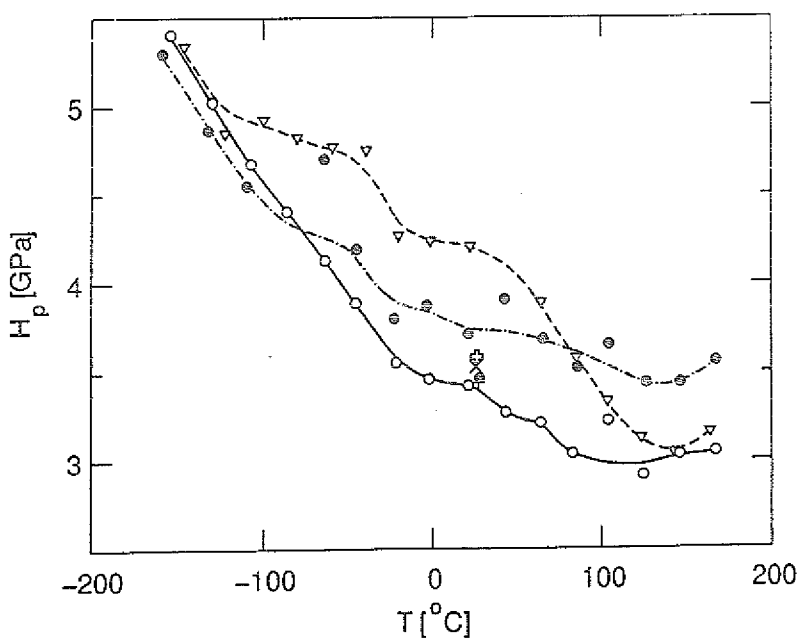

Fig.20: Microhardness (maximum load 1 N) versus temperature of MANET I specimens irradiated at 520°C with 6.2 MeV protons to a dose of 0.55 dpa (▽), and of specimens implanted at 600°C with 33 (o) and ≈1000 atppm (●) helium. Crosses indicate measurements at the unirradiated end pieces.

Most of the above measurements were, in addition to the 136° Vickers indenter, also performed with a sharper square pyramid indenter of 90° apex angle. Some of these results are sketched in figure 21. The measurements before and after implantation and after 450°C annealing show no effect of indenter angle within experimental scatter. But after 650°C annealing the hardness determined by the 90° indenter is even increased compared to 450°C (dash-dotted lines), while the data of the 136° indenter (solid lines) go back to the values before implantation. In contrast the 185 atppm specimen show this increase in hardness from 450° to 650°C annealing only at temperatures above -20°C (figure 22).

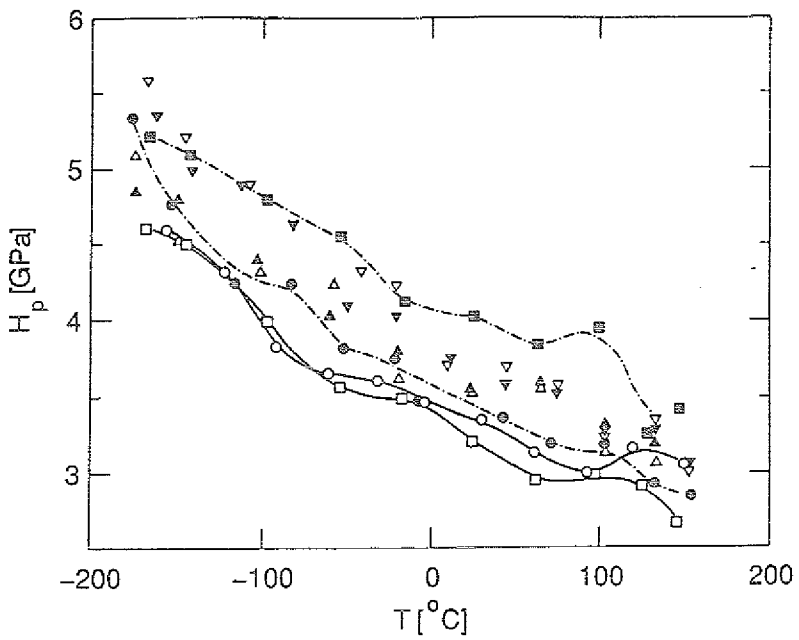

Fig.21: Microhardness (maximum load 1 N) versus temperature of specimens before (o) and after (▽) implantation of 36 atppm He and after annealing to 450° (△) and 650°C (▣). Full and empty symbols indicate indenters of 90° and 136° apex angle, respectively.

The measurements of Young's modulus during unloading show a slight decrease with increasing temperature, and only a minor effect of irradiation as well as implantation. According to figure 23 the implantation induced (185 atppm He) increase of E diminishes from about 10% to 0% when temperatures is raised from -160° to +160°C. On the other hand the irradiation induced (0.11 dpa) increase of E is only 10% at -160°C and increases to 20% at +160°C. No significant effects are found after irradiation or implantation at elevated temperatures.

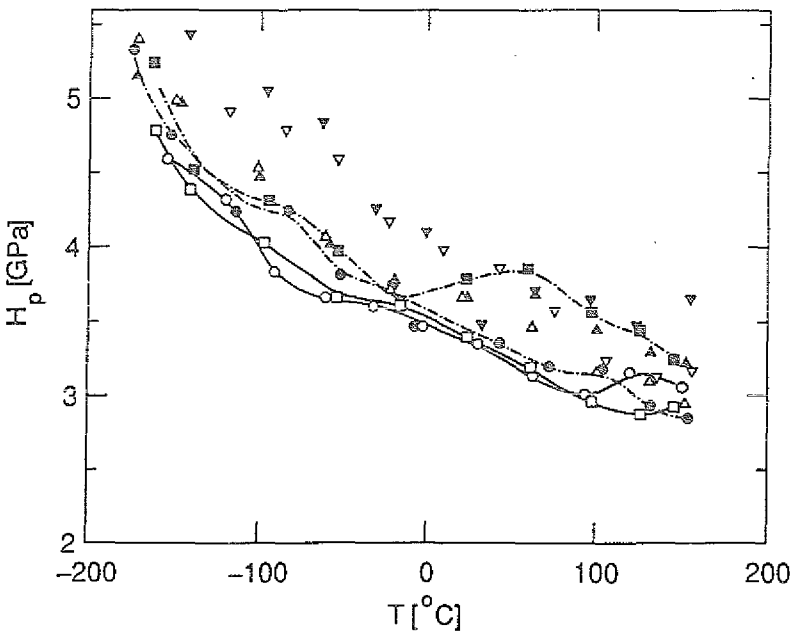

Fig.22: Microhardness (maximum load 1 N) versus temperature of specimens before (o) and after (▽) implantation of 185 atppm He and after annealing to 450° (△) and 650°C (□). Full and empty symbols indicate indenters of 90° and 136° apex angle, respectively.

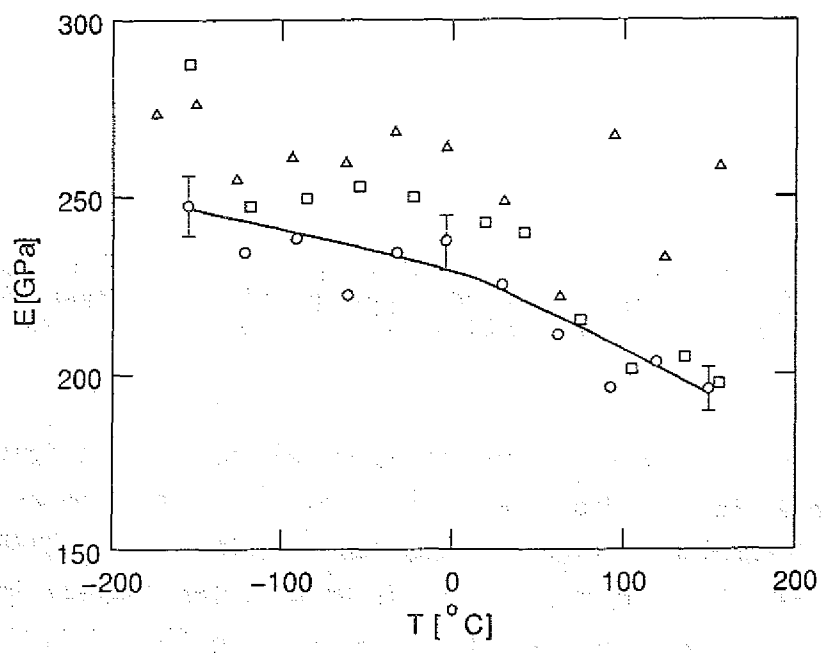

Fig.23: Young's modulus of MANET II before (o) and after irradiation to 0.11 dpa (△) and implantation to 185 atppm He (□), respectively.

5.2. Irradiation effects on braze junctions

In future fusion reactors braze junctions will be used for joining some of the structural components and for fixing plasma facing materials like carbon to metallic heat sinks, e.g. for divertor applications. Investigations of irradiation effects on the properties of brazed junctions are performed at C.E.-Saclay including a cooperative study on hardness.

5.2.1. Stainless steel brazings

The specimen consisted of two 316 stainless steel plates brazed by a Ni-base alloy containing ≈14 wt% Cr, 0.2 wt% Fe and 10% phosphorus (BNi7) at 1200 to 1366 K in vacuum [71]. The specimen were 3 mm diameter discs cut perpendicularly to the junction and surfaces were either polished with 0.25 μm diamond paste or by ion milling (5 keV Ar^+). It turned out that the results of the following investigations were not affected by the specific polishing technique. The specimens were irradiated with 500 keV Ni ions at temperatures of 303 and 523 K in a Van de Graaff accelerator at SRMP, C.E.-Cadarache [72] to a displacement dose of ≈10 dpa.

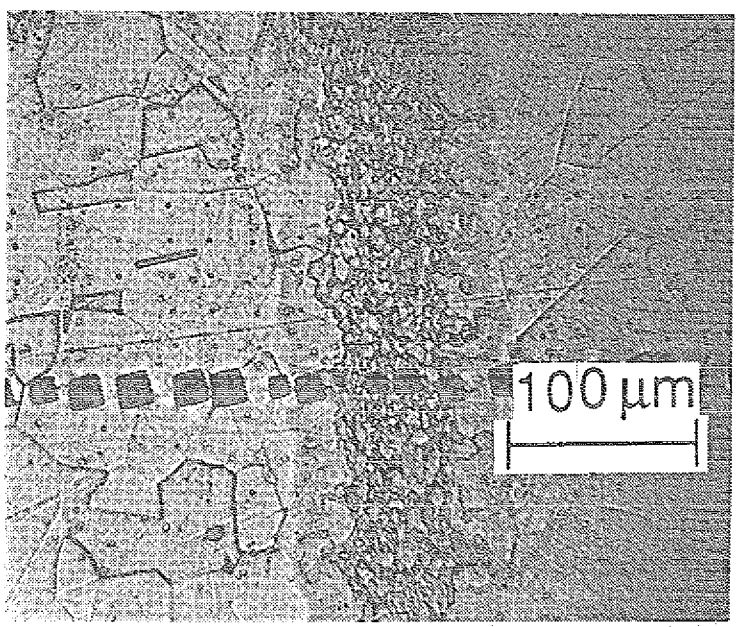

Fig.24: Optical image showing the arrangement of indentations on a cross section of stainless steel plates and an intermediate braze region. The large indentations are markers, while the small squares are the measuring indentations.

Microhardness and Young's modulus were determined in the braze region and in the adjacent stainless steel plates with a Vickers indenter at room temperature, at a maximum load of 0.015 N, a loading rate of about 20 nm/s and zero holding time. The arrangement of indentations on the braze and adjacent stainless steel is shown in fig. 24. Typical penetration depths were 300 nm (Vickers diagonal ≈ 2 μm) which is slightly more than the maximum range (≤300 μm) of the 500 keV Ni ions. This means that the measured hardness is dominated by the implanted region and only minor contributions may come from the unimplanted part underneath, as

has been shown by theoretical calculations [21] and the investigations on thin films in chapter 5.3. In the braze region two different load versus depth curves were observed: one has a shape typical for metals, cf.fig.3a, while the other shows more curvature of the unloading curve, resembling the behaviour of hard materials, cf.fig.3b. Figure 25 shows typical load versus depth curves from the stainless steel and from a high-hardness point in the braze region.

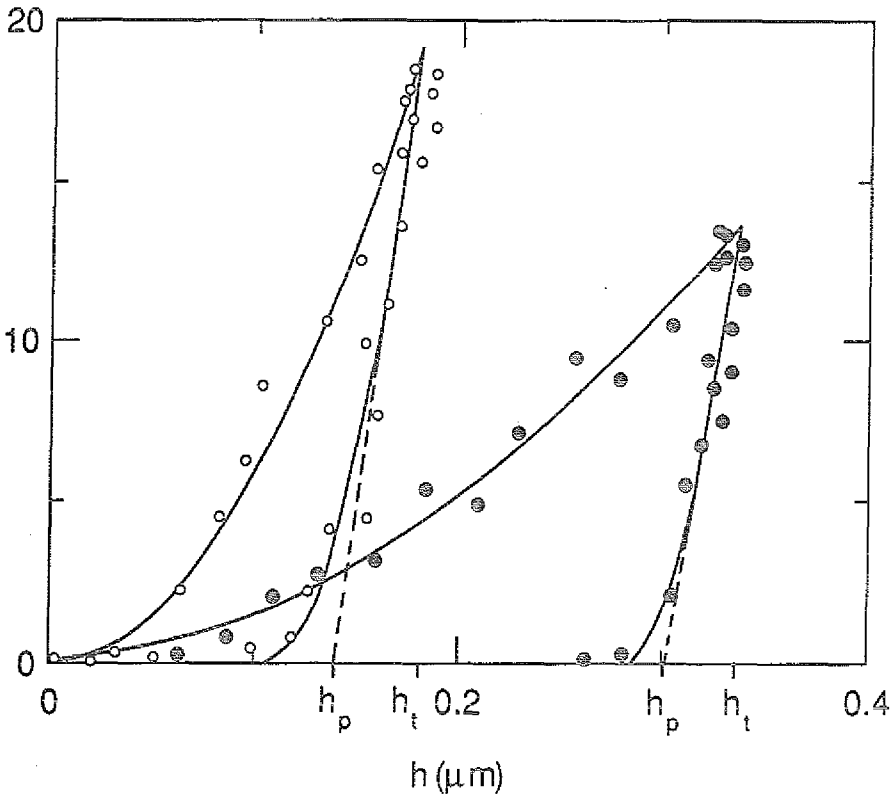

Fig.25: Load versus depth curves from the stainless steel (-) and the braze (o) region.

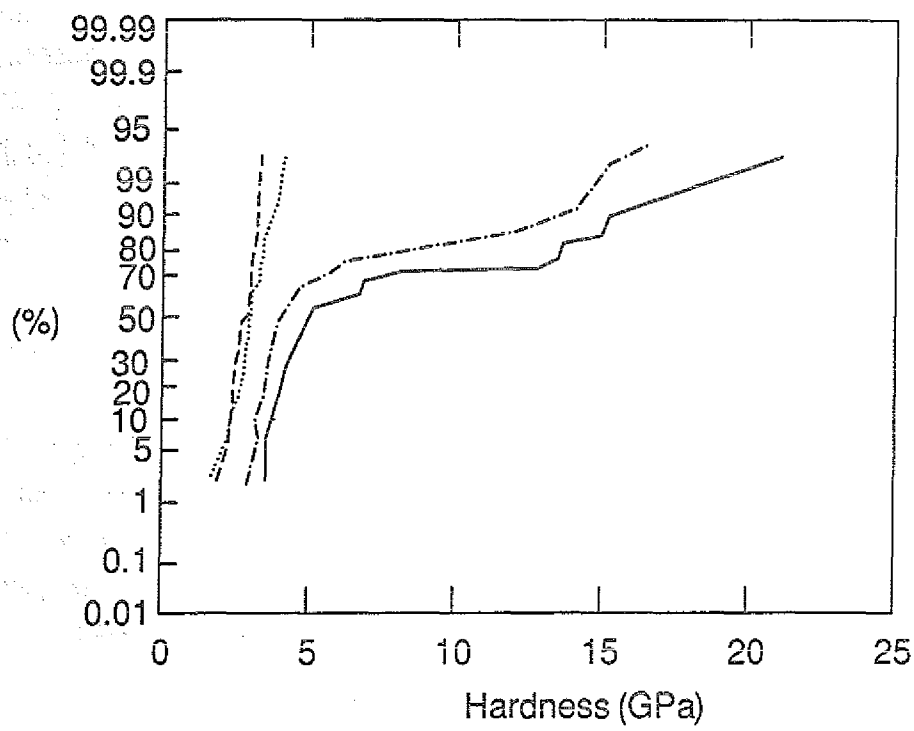

Fig.26: Integrated hardness distribution in the stainless steel (left curves) and in the braze (right), before (--,-) and after (•••,-••) irradiation

The hardness values in the braze show a much wider distribution than in the steel. Figure 26 shows the integrated hardness distributions in both regions, i.e. the fraction of hardness values which are below a given value on the abszissa: In the steel the distribution is close to a Gaussian with an average value of 2.5 GPa (--), while in the braze only about 50% of the indentations show a narrow distribution around 4.5 GPa while the rest shows a very broad distribution, extending to values beyond 20 GPa (-). A possible explanation is that in the braze region there are at least two different phases with different hardness. This was confirmed by microprobe analysis which revealed a nickel rich solid solution and a M_2P phosphide [72]. The lower (about 70% of the data) and the higher hardness values probably belong to the solid solution and to the phosphide phase, respectively. The intermediate hardness values may be an average of the hardness of small phosphides and matrix, weighted by a geometrical factor which depends on the relative volume fractions and the depth of the phosphide in the indentation volume. Data on Young's modulus are given in figure 27, showing large data scatter with significant higher values in the braze than in the steel.

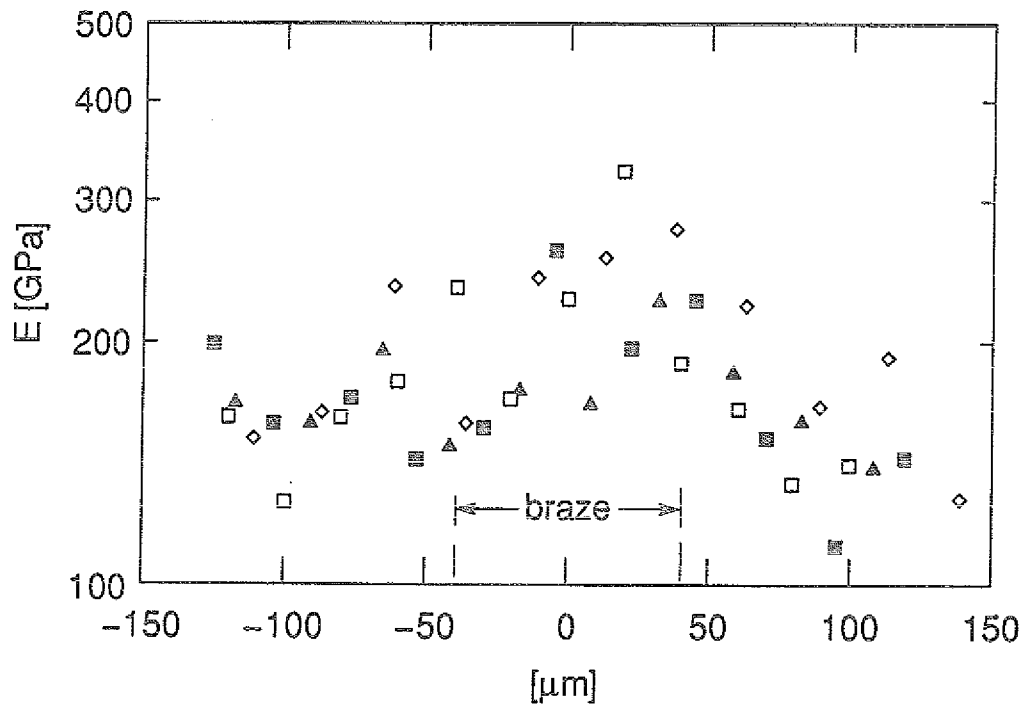

Fig.27: Young's modulus measured across the braze junction between stainless steel plates before (□,◇) and after irradiation at room temperature (▣) and at 523 K (▲).

Included in fig.26 are integrated distribution of hardness values after 500 keV Ni irradiation to a dose of 10 dpa in the stainless steel (•••) and in the braze (-•-), respectively. The stainless steel shows some slight hardening which does not depend significantly on irradiation temperature, possibly due to the

formation of a dislocation network which is rather insensitive to irradiation temperature [73,74]. In the braze region, the first steep part of the curves which probably corresponds to the nickel base solution shows no significant effect of irradiation, while the high-hardness part, which possibly describes the phosphide phase, shows softening (e.g. amorphisation) due to irradiation. It may be caused by softening or dissolution of the phosphide phase under irradiation [72]. Also the irradiation effects in the braze show no significant dependence on irradiation temperature. Young's modulus does not show any change in both regions by irradiation.

5.2.2. Carbon-to-metal brazings

Carbon was brazed by CuAgTi braze metals to copper and molybdenum, respectively. The surfaces were prepared by polishing with SiO_2 of grain size smaller than 0.1 µm. Figure 28 shows SEM pictures of the Cu/C and the Mo/C brazed regions with the indentations. EDX analysis in the SEM with a beam of 20 nm diameter allowed to assign hardness values to the different regions. At least two phases in the C/Cu braze region and at least four clearly different compositions in the C/Mo braze region were found, see table V. Microhardness was tested with a maximum load of 0.01 N, giving depths from 0.25 to 0.6 µm, depending of the area investigated. Figure 29 shows typical loading/unloading curves from different regions of the Mo/C braze. Copper shows within a distance of about 50 µm from the braze a heat affected zone which contains a few percent of Ag and Ti. In this zone hardness shows a characteristic variation with distance from the braze with a peak about 20 µm from the braze, see figure 30. Such an effect was not observed in molybdenum.

Table V: Composition, typical location and appearance in the SEM and hardness values of major compositional varieties in the Mo/C and Cu/C brazes.

	composition	location/SEM-appearance	hardness [GPa]
Cu/C			
	100%Cu	bulk metal	1.3±0.3
	100%Cu	heat affected zone	1.5••2.4
	60-70%Ag,20-40%Cu	bright areas in the braze	1.5±0.3
	≈65%Cu,30%Ag	dark areas in the braze	1.4±0.5
Mo/C			
	100%Mo	bulk metal (TZM)	3.1±0.7
	50-80%Cu,20-50%Ti	dark islands along Mo boundary	2.7±1.5
	70-80%Ag,17-25%Cu	bright areas in the braze	1.2±0.4
	96%Cu,2-3%Ag	dark areas in the braze	1.5±0.4
	45-60%Cu,35-55%Ti	rim along C boundary	3.4±1.6

A major problem in both cases is the evaluation of the measurements on carbon as this material shows a strongly curved unloading curve which almost parallels the loading curve, i.e. almost complete recovery occurs (see fig.29). Therefore the linear extrapolation of the initial part of the unloading curve for the determination of h_p (cf. fig.2) is difficult and the derivation of hardness and Young's modulus rather ambiguous.

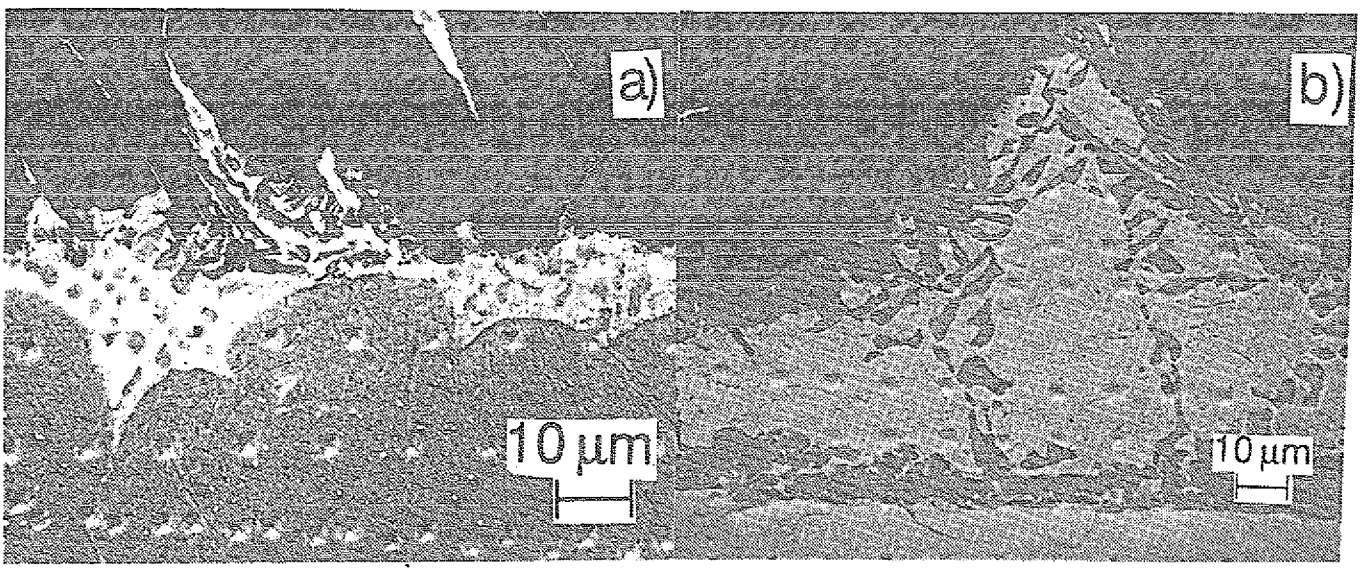

Fig.28: SEM (20 kV) pictures of the brazed region between metal (bottom) and carbon (top, dark) in Cu/C (a) and Mo/C (b) showing the indentations.

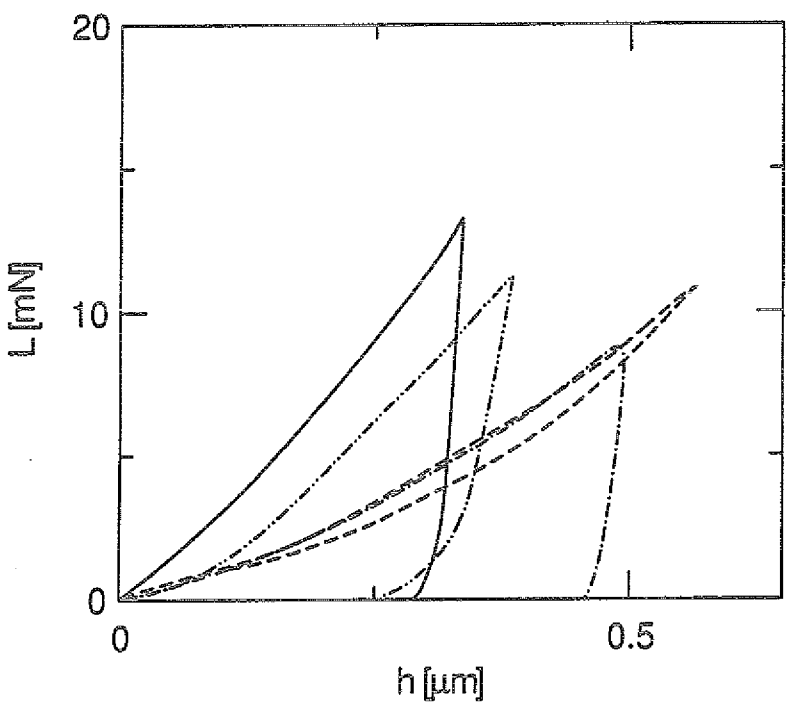

Fig.29: Typical loading/unloading curves of molybdenum (-), bright (-••) and dark (-•••) region in the braze and graphite (--) before irradiation.

The specimens were irradiated with 700 keV Kr^{++} ions at room temperature and at 673 K to doses of about 10 dpa. Only subtle if any effects of irradiation on hardness were observed, cf. fig.30. Furthermore the variations in the hardness values observed for the individual "phases" was so large (see error margins in table V) that minor changes cannot be safely assigned to irradiation. This results on hardness of brazed regions will be supplemented by investigations of other properties at C.E. Saclay.

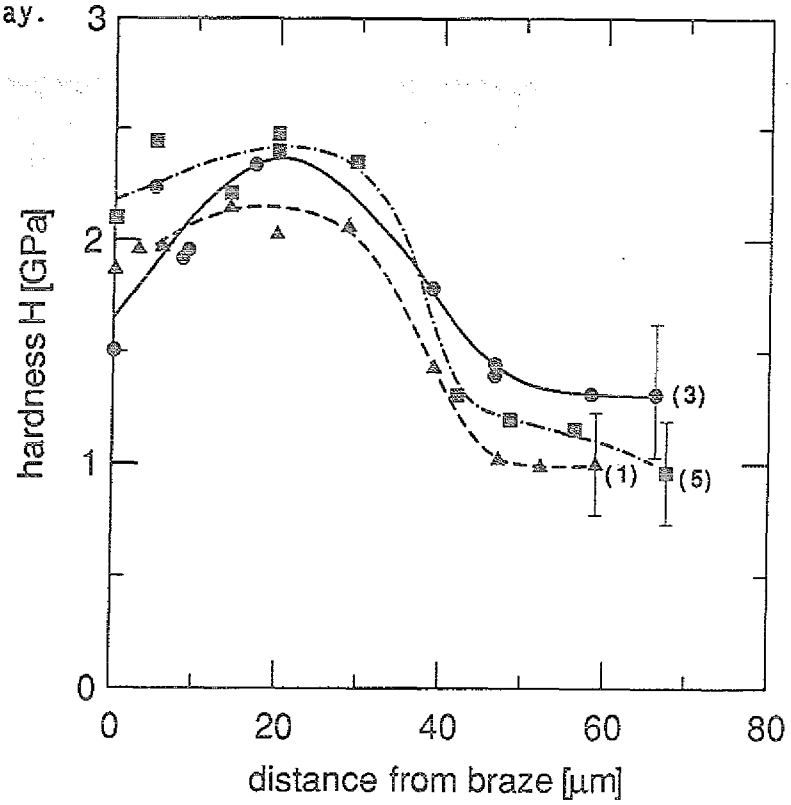

Fig.30: Variation of hardness of copper towards the braze boundary before (●,—) and after irradiation at room temperature (▲,--) and 673 K (■,-·-).

5.3. Investigation of thin metal films on insulators

Metallic films on semiconductor substrates are used for current leads on microelectronic devices. Cooling from the elevated temperatures, used for film production, induces thermal stresses which can cause disintegration of the films. Integral information on the stresses in the films (index f) of thickness t_f can be obtained by measurement of the radius R of curvature of the substrate (index s) [75-77]:

$$\sigma=(1-E_f t_f/E_s t_s)\cdot(E_s/(1-\nu_s))\cdot t_s^2/(6\cdot R\cdot t_f) \qquad (12)$$

Submicron hardness testing is used in an attempt to investigate the elastic and mechanical properties of the film material as a function of distance from the interface. Previous studies on this topic for example included 0.2 to 1.1 µm Al films on a SiO_2/Si substrate [75], 1 to 3 µm Al films on Si [78,79], 0.06 to 0.4 µm W films on Si [9,75], also polymers on Si [80,81], hard coatings on metals

[24], and implanted layers on steel [82]. As already mentioned, the microhardness of homogeneous materials is related to flow stress by $\sigma_y \approx H/3$ or by more detailled relations including work hardening [83,84]. Determination of film properties from straightforward assumptions like a linear superposition of the hardnesses of film and substrate as proposed in ref.[22] may be oversimplified and elastic modulus [9] and hardness [21] of the film must rather be derived from more involved relations.

Aluminum films of 0.4, 1.6 and 4.0 μm thickness were prepared on vitreous silica by evaporation. Details of specimen preparation and characterisation has been given elsewhere [77]. Figure 31 shows normalized load versus depth curves for 1.6 μm aluminum films. There appears a marked change in the shape of the curves, mainly during unloading. At small indentation depth (solid line) the loading curve shows slightly less curvature, due to some linear part in agreement with the observation in the studies on ISE (chapter 4). The unloading curve is steep at small indentations as expected for metals, see chapter 4, and becomes flatter with increasing depth, due to the increasing contribution of the hard substrate. Hardness data from films of 0.4, 1.6 and 4.0 μm and bulk material as a function of indentation depth h_p are given in figure 32 for indenters of α=68° (Vickers) and 80.5°. At least the 1.6 and 4.0 μm films show almost constant hardness over a wide range of depths. Only at depths around the film thickness, hardness starts to increase due to the contribution of the substrate. At large depths the hardness measurements for hard substrate covered by a soft film can be tentatively described by subtracting the film thickness from indentation depth as proposed in [85]:

$$H_S = 2L/(d^2 \cdot (1-t_f/h_p)^2) \qquad (13)$$

This relation is plotted in fig.32 by the dash-dotted lines, assuming H_S=9.8 [GPa] as obtained for SiO_2 in chapter 5. This relation fits the measurements on the 1.6 μm film with the 68° indenter quite well, while for the two other films a better fit would be obtained by assuming thicknesses of 0.2 and 3.5 μm instead of the given values of 0.4 and 4.0 μm, respectively. While details of the fit are certainly influenced by the values of t_f and H_S, nevertheless systematic deviations from equation (13) exist. For example, at $h_p \gg t_f$, equation (13) predicts a dependence of $2L/d^2$ on h_p for equal t_f which is independent of indenter shape. This is certainly not the case. Especially the data from the 1.6 μm film with the 80.5° indenter do not show any increase in hardness at depths much larger than the film thickness and also the t_f=0.4 μm data show systematic deviations.

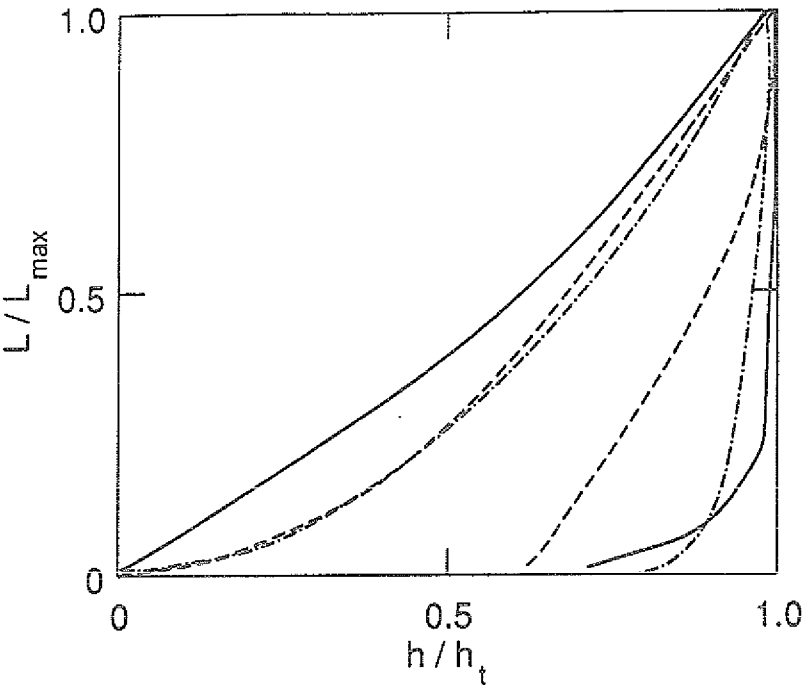

Fig.31: Normalized loading/unloading curves with α=68° (Vickers) indenters on 1.6 μm Al films on vitreous silica. Maximum loads [mN] and indentation depths [μm] were 4.0, 0.43 (-), 76., 1.9 (-·-) and 500., 4.3 (--), respectively.

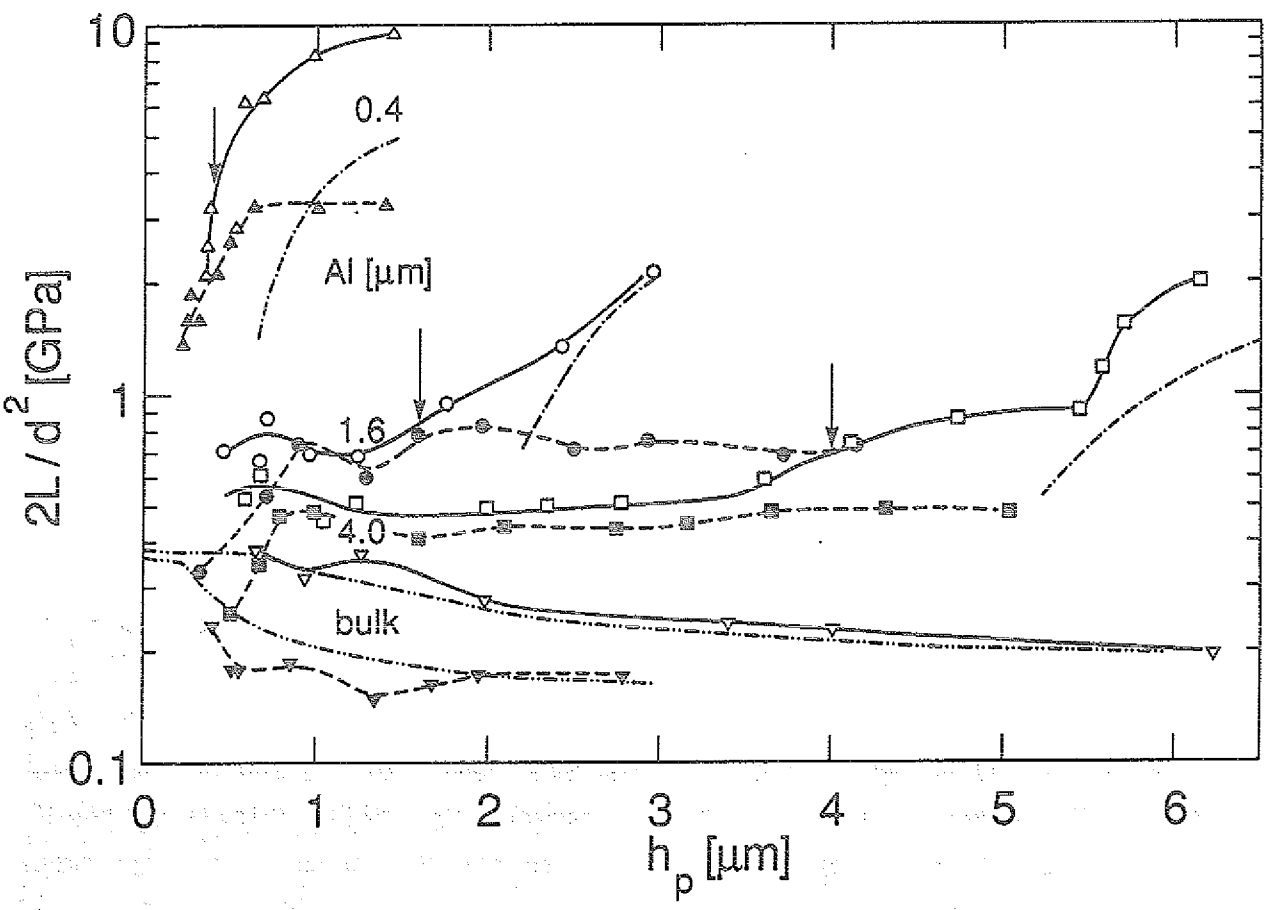

Fig.32: Hardness versus depth curves of aluminum films of 0.4 μm (△), 1.6 μm (o), 4.2 μm (□) and >2 mm (▽) thickness on vitreous SiO_2 substrates. Open and filled symbols indicate indentations with square pyramid indenters of 68° (solid lines) and 80.5° (dashed lines) halfapex angles. The arrows indicate the thicknesses of the Al films. The dash-dotted lines correspond to equation (13) with H_S=9.8 [GPa] and the dash-double-dotted lines describe the indentation size effect of Al according to equation (8).

The results in figure 32 clearly show that the "hard"substrate becomes noticeable only at indentation depths greater than the film thickness. This is in good agreement with theoretical calculations [21], while previous measurements found this limit even at slightly higher depth [86].

In Figure 33 the hardness values taken at $h_p=t_f/2$ are plotted versus reciprocal film thickness. For the 0.4 μm film no plateau of hardness could be detected within the minimum depth (≈200 nm) of the present instrument and the respective value must therefore be considered as an upper limit. Included in fig. 33 are data from ref.[75] which are in reasonable agreement with the present results, except for that 0.4 μm data point. A reciprocal dependence on thickness (σ_F[MPa]=18+131.3/t_f[μm]) has also been found for the flow stress σ_F as determined by bending measurements [77] in agreement with previous studies [75,76]. A plot of σ_F versus hardness is given in figure 34. For a detailled analysis also the effect of grain size on flow stress must be taken into account, as it is almost impossible to keep grain size constant in films of different thicknesses. But it has been shown in refs.[75,77] that a Hall-Petch type grain size dependence with the parameters of aluminum cannot explain the thickness dependence of flow stress, despite there is some effect. Theoretical descriptions of the flow stress of thin films have been discussed in detail in ref.[77].

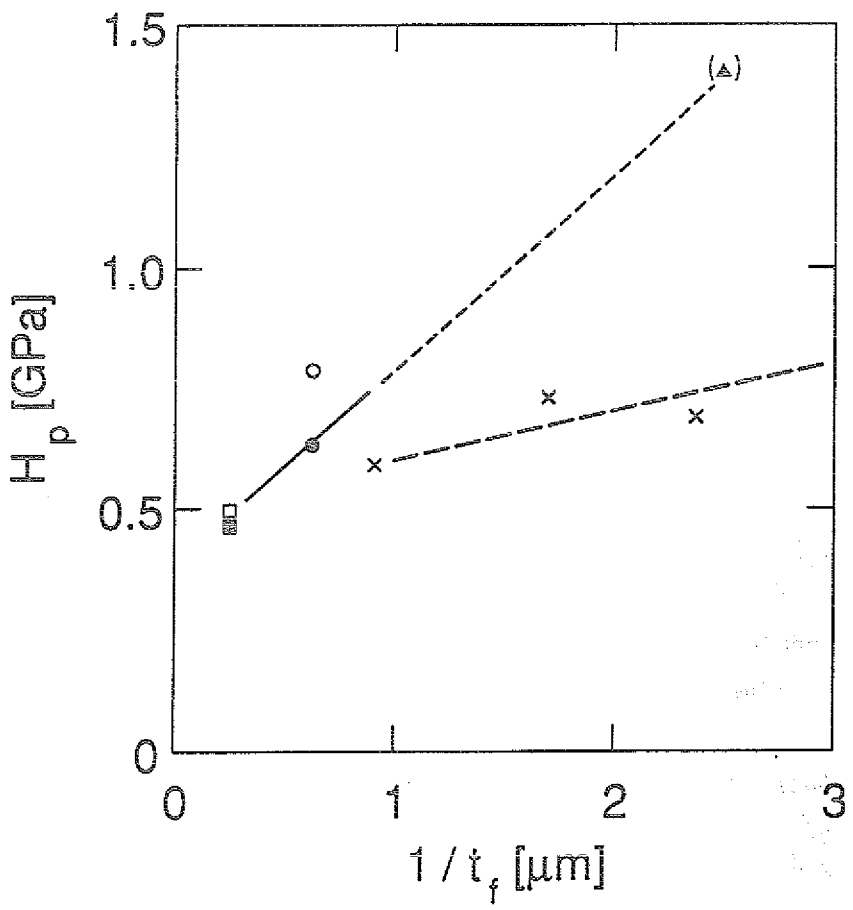

Fig.33: Dependence of the hardness of Al films on vitreous SiO_2 on reciprocal thickness. Symbols as in fig.32. Crosses (x) indicate results on Al films on Si from ref.[75].

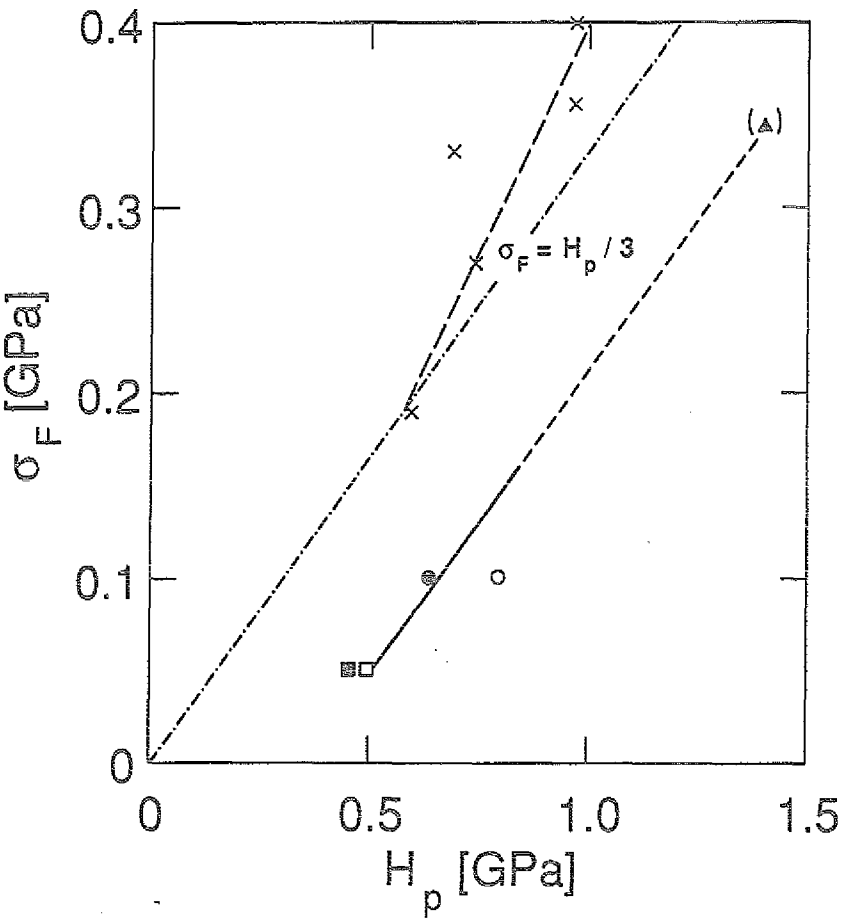

Fig.34: Flow stress σ_F derived from bending tests versus hardness H_p. Symbols as in fig.32. Included are results from ref.[75] (x), and the relation $\sigma_F = H_p/3$ (---).

5.4. Elastic properties of oxide films on SiC ceramic

There are certain applications which call for protective layers on ceramic materials, e.g. oxide films on SiC which are produced by steam oxidizing. The characterisation of these layers includes measurement of elastic properties which can be done after peeling off the films or in-situ by instrumented microhardness testing. In the present investigation oxide layers of about 10 μm thickness were tested by submicron indentation at room temperature with loads of 0.01 to 0.11 N, giving indentation depths of $\leq$0.7 μm, i.e. much smaller than the estimated oxide thickness. Hardness values H_p of 9.8±1 [GPa] and Young's modulus E of 74±2 [GPa] were obtained, both virtually independent of load. The E-value is in very good agreement with literature data of vitreous silica, see ref.[31], while on the other hand for SiC, E-values around 400 GPa are reported. This results identify the oxide layer as vitreous SiO_2 and indicate that its elastic modulus is neither affected by the small thickness nor by the underlying bulk SiC.

5.5. Indentation creep

The term 'indentation creep' is used for measurements of the time dependence of indentation under constant load. Actually this type of measurement is closer related to stress relaxation than to creep. As already mentioned, in indentation experiments with linear indenters like pyramids and cones, strain is constant $\approx 0.2 \cdot \cot\alpha$ [6], while during progressive indentation under constant load, stress is decreasing due to the increasing support area. The major difference to an uniaxial stress relaxation test is the increase of the deformed volume when the indenter is penetrating. In the following only some experimental results will be given, while a discussion on the basis of dislocation behaviour would be rather involved, cf. the respective articles in handbooks on creep and stress relaxation.

Figure 35 shows the load versus depth curves of 1 mm thick specimens of 99.999% aluminum from VAW, Germany, during indentation creep with a Vickers indenter at a load of 0.5 N for 18 hours at 105° and 265°C. The load is kept constant to better than 1% by electronic control. As already shown in Figure 3a unloading of Al produces negative load, probably due to some "sticking" of the indenter to the specimen. The depth reached after load application was in the following subtracted from the total depth and only the penetration increment $\triangle h_t$ is plotted in the figure 36 as a function of holding time.

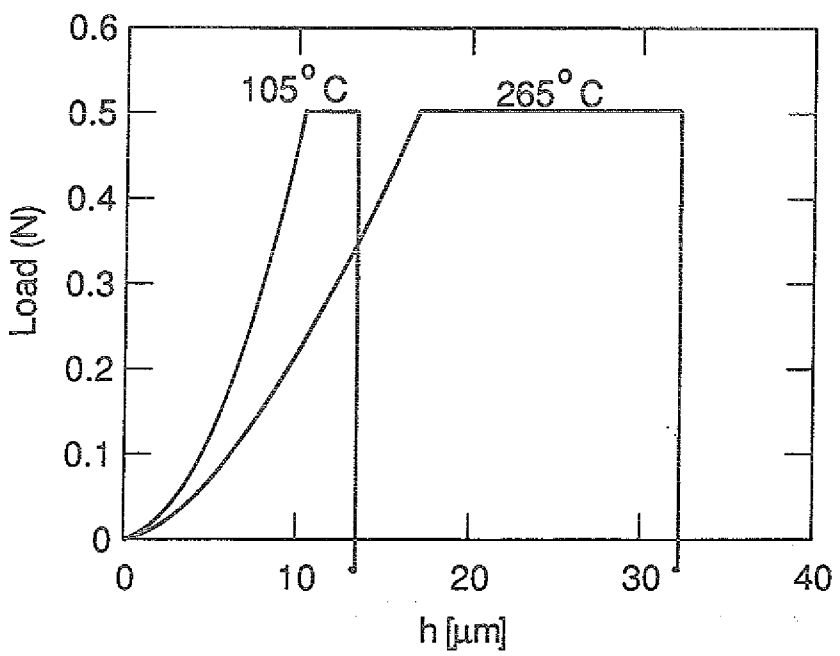

Fig.35: Load versus depth curves of 1 mm thick specimens of 99.999% Al during indentation creep with a Vickers indenter at a load of 0.5 N for 18 hours at 105° and 265°C.

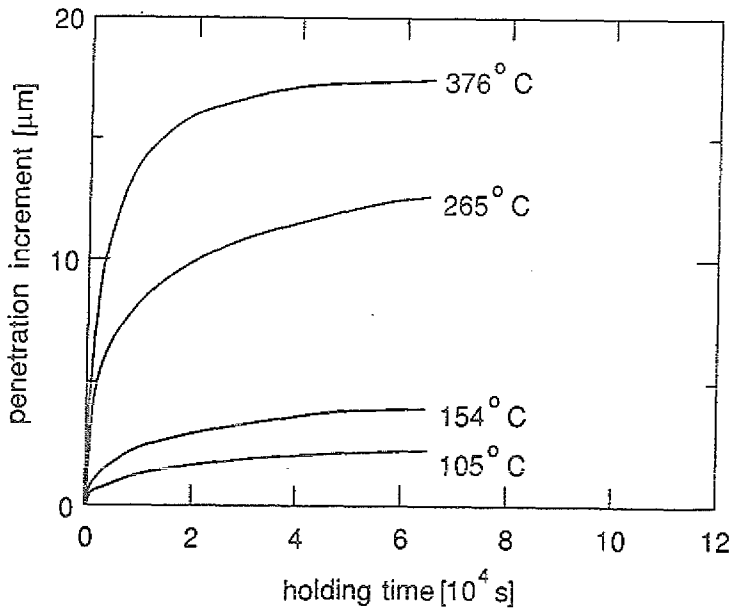

Fig.36: Indentation creep curves of 99.999% Al under a constant load of 0.5 N. The penetration increments were derived by subtracting the penetration depths during first loading [μm] of 10.45 (105°C), 12.75 (154°C), 17.03 (265°C) and 23.33 (376°C) from the total depths.

The standard approach to describe stress relaxation assumes that elastic strain σ/E is continuously transformed to plastic strain ϵ_p, such that the total strain ϵ remains constant:

$$\epsilon = \sigma/E' + \epsilon_p \qquad (14)$$

The elastic modulus E′ comprises contributions from the specimen and from the testing device. In conventional stress relaxation experiments the testing device makes a large and often not precisely known contribution to the strain and thus causes appreciable uncertainties. In this respect the present set-up has big advantages as the strain measurement by capacitance directly at the specimen surface avoids almost any extraneous contributions and E′ is very close to E. If the plastic strain rate is derived from a steady state creep relation:

$$\epsilon_p = B \cdot \sigma^n \cdot t \qquad (15)$$

one obtains by integration:

$$\sigma^{-(n-1)} - \sigma_0^{-(n-1)} = (n-1) \cdot B \cdot E \cdot t \qquad (16)$$

With the relation between stress and indentation depth, given by equation (2a), the following time dependence of depth is obtained:

$$h^{2(n-1)} - h_0^{2(n-1)} = (n-1) \cdot B \cdot (L \cdot \cot^2\alpha/4)^{n-1} \cdot E \cdot t \qquad (17)$$

t=0 and h_0 were taken when the load L was applied and it was tried to fit equation (17) to the present data. Literature data on the stress exponent n of Al concurringly give values around n=4.4 [87]. But even for other values of n, equation (17) does not fit the present data. Therefore equation (15) was replaced by a transient creep equation. Transient creep is usually desribed by expressions given by Andrade [88]:

$$\epsilon_p = C \cdot \sigma^n \cdot t^{1/3} \tag{18a}$$

or by McVetty [89]:

$$\epsilon_p = C \cdot \sigma^n \cdot (1 - e^{-t/\tau}) \tag{18b}$$

A general description of transient creep of pure aluminum has been given in ref.[90] using data from ref.[91], yielding $C \cdot \sigma^n = 0.105$ and $\tau^{-1} = 82 \cdot \epsilon_s$, where ϵ_s is the stationary creep rate. The latter can be described [92] by:

$$\epsilon_s = 3.5 \cdot 10^{-19} \cdot \sigma^n \cdot e^{-Q/kT} / T \tag{19}$$

where n=4.4 and Q=1.56 eV.

Integration of equations (14) and (18a) or (18b) yields:

$$\sigma^{-(n-1)} - \sigma_0^{-(n-1)} = (n-1) \cdot C \cdot E \cdot (t^{1/3} - t_0^{1/3}) \tag{20a}$$

$$\sigma^{-(n-1)} - \sigma_0^{-(n-1)} = (n-1) \cdot C \cdot E \cdot (e^{-t_0/\tau} - e^{-t/\tau}) \tag{20b}$$

and correspondingly:

$$h^{2(n-1)} - h_0^{2(n-1)} = C \cdot (n-1) \cdot (L \cdot \cot^2\alpha/4)^{n-1} \cdot E \cdot (t^{1/3} - t_0^{1/3}) \tag{21a}$$

and

$$h^{2(n-1)} - h_0^{2(n-1)} = C \cdot (n-1) \cdot (L \cdot \cot^2\alpha/4)^{n-1} \cdot E \cdot (e^{-t_0/\tau} - e^{-t/\tau}) \tag{21b}$$

The present treatment implies that plastic deformation results from elastic strain, cf.equation (14), and that the deformed volume which relaxes according to equation (18) is constant. A basically different point of view was taken in ref.[93] where the plastic deformation strain rate and the relative increase of the radius of the deformed volume was set proportional to the penetration rate, while the contribution of elastic forces was neglected. For strain equation (18a) this attempt gives an expression slightly different from equation (21a):

$$h^{2n} - h_0^{2n} = C' \cdot n \cdot (L \cdot \cot^2\alpha/4)^n \cdot (t^{1/3} - t_0^{1/3}) \qquad (22)$$

where $C' \approx C$ within a factor of about 3. A discrimination between the two transient creep equations (18a) and (18b) was tried by fitting of equations (21a) and (21b or c) to the indentation creep curves as shown for example in fig. 37. In such a plot a linear relation is expected from these equations. In fig.37 the n=6 curves, if any, fulfills the demand of linearity. Fits of equation (21b) come closer to linearity, but with unreasonably large τ values, which in addition are almost independent of temperature, in contrast to equation (18b) which suggest an activation energy for τ equal to that of steady state creep, i.e. values from 1.21 to 1.54 eV as obtained from conventional creep experiments [94].

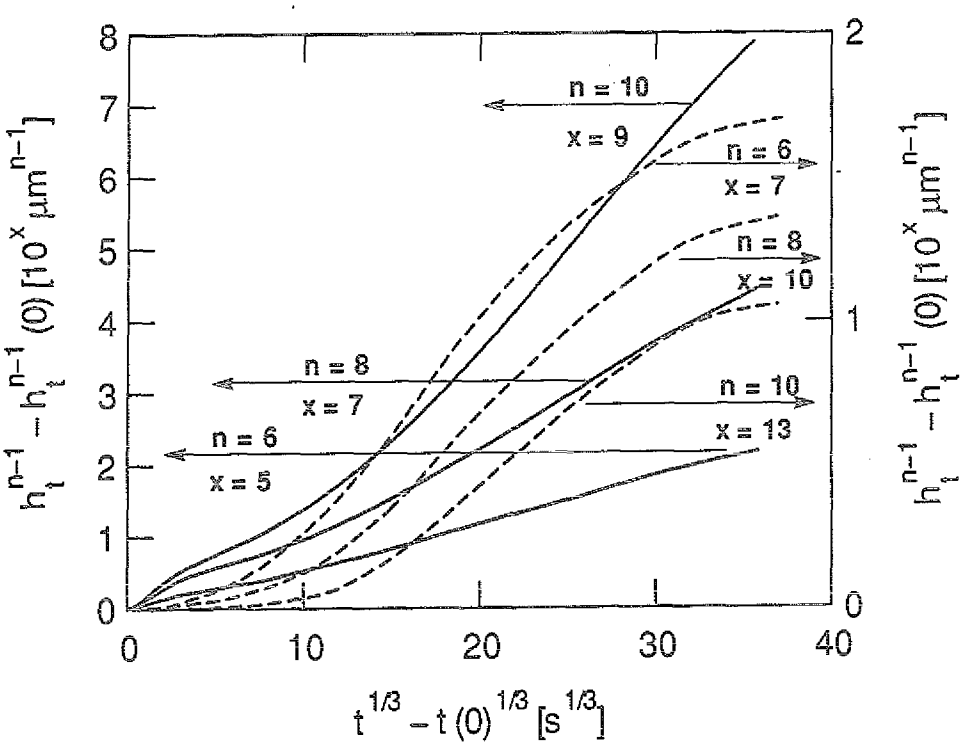

Fig.37: Fit of the indentation creep curves at 105°C (solid, left ordinate and 265°C (dashed, right ordinate) of fig.36 to equation (21a). n is the stress exponent in equation (18a) and x is the exponent of the scale on the ordinates.

Indentation creep measurements were also performed on type DIN 1.4914 martensitic stainless steel (MANET II) which showed only very small penetration increments, cf.fig.40.

5.6. Indentation fatigue

Recently repeated indentation has been proposed as a method for studying fatigue effects in ceramics [95,96]. The impression fatigue test has also been applied to metals using a cylindrical flat end indenter [97]. But only the advent of automatic, fully instrumented microhardness testers makes indentation fatigue a viable tool for material science. It will be shown in the following that this adds an attractive facet to the possibilities of an instrumented microhardness tester. Figure 38 schematically shows the load versus time dependence in an indentation fatigue test with maximum and minimum loads of 0.5 and 0.1 N, respectively, with holding times of 10 seconds on both levels. From an experimental point of view the indentation fatigue test is a push-push fatigue experiment at constant strain, as given by the indenter angle, under a stress which is decreasing as pentration proceeds. As already set out in the context of indentation creep this means that indentation fatigue actually is a cyclic stress relaxation test under intermittent loading.

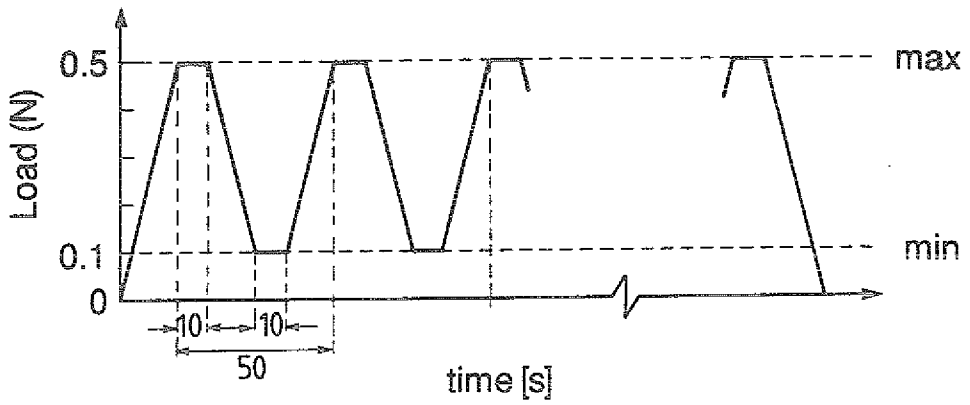

Fig.38: Schematic view of the loading program in an indentation fatigue test.

Figure 39 compares indentation fatigue to indentation creep results on 99.999% Al at 0.5 N load around 106° and 371°C. For the fatigue test the total cycling time is given. The penetration depth in the fatigue test was measured at maximum load. While at 106°C the deformation in the indentation fatigue test is slightly higher than under constant load, the deformation found around 371°C under cyclic loading is much smaller. One remarkable feature is that the penetration increment even is slightly reduced after about 300 cycles (15000 s).

Indentation fatigue tests were also performed at -100°C, 0°C and 80°C with a quadratic pyramid indenter of 88.2°apex angle on MANET II martensitic stainless steel (cf.table II) which was polished by 1 μm diamond paste. In figure 40 the fatigue results are compared to indentation creep at 80°C also by the 88.2° indenter with 0.5 N constant load. The penetration depth in the fatigue test was

again measured at maximum load. The most prominent result is the much larger penetration depth in the fatigue test than in the creep test even with the maximum load of 0.5 N kept only for 1/5 of the total cycling time. Furthermore the penetration increment at 80°C is slightly smaller than at 0°C. The increase in area during proceeding penetration at constant load can be converted to a decrease in stress, giving reduction of strength by 22% (-100°C), 26% (0°C) and 25% (80°C) after the 1000 cycles fatigue tests, respectively, but only 2% reduction after the 15 hour creep test.

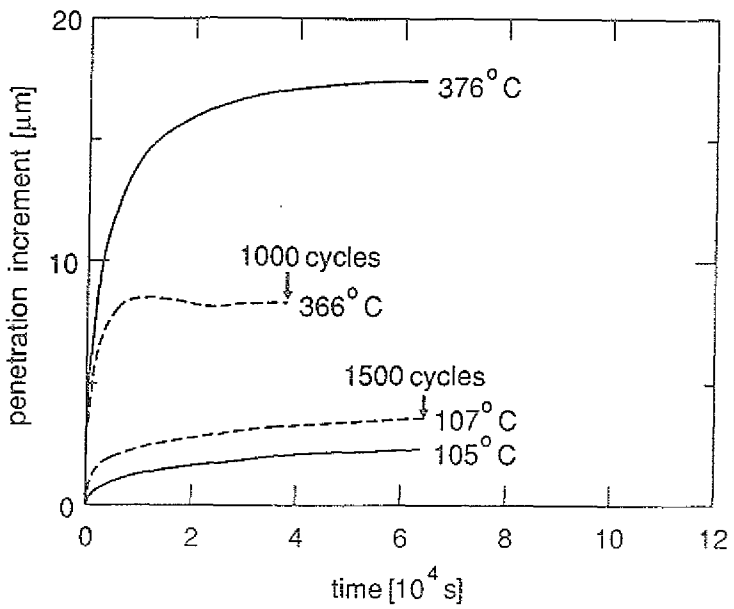

Fig.39: Comparison of indentation fatigue (dashed) to indentation creep (solid) results on 99.999% Al at 0.5 N around 106° and 371°C. In contrast to fig.38 the holding times were only 5 s. The instantaneous depths [μm] in the fatigue tests were 12.25 (107°C) and 21.08 (366°C), respectively, while those of the creep test are given in fig.36.

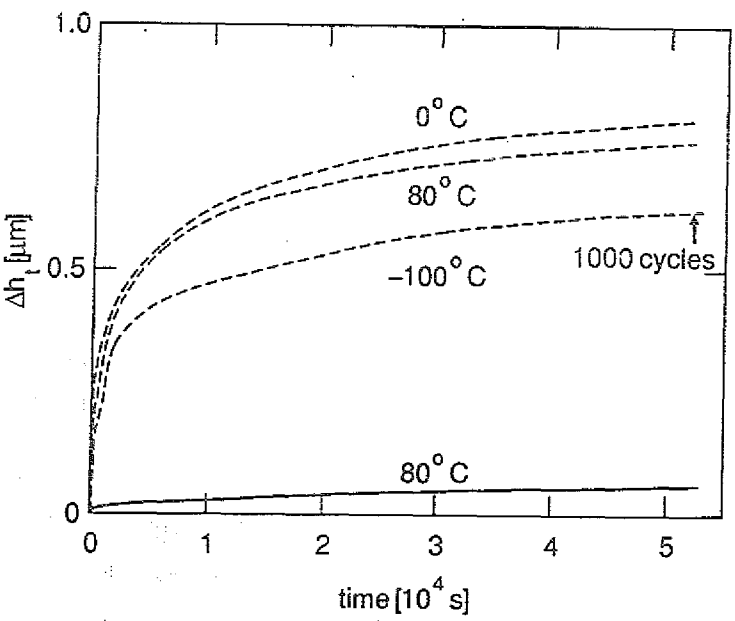

Fig.40: Comparison of indentation fatigue (dashed) to indentation creep (solid) results on MANET II martensitic stainless steel at 0.5 N and temperatures as indicated. The instantaneous depths [μm] in the fatigue test were 5.69 (-100°C), 5.96 (0°C) and 6.47 (80°C), and 6.27 in the creep test.

The indentations after the indentation fatigue and creep tests were investigated by SEM. The SEM pictures from fatigue tests showed no significant variation with temperature. The pictures from test at 80°C are shown in figure 41. Both show some pile-up around the indentation but no visible cracks. Some of the fatigue indentations (fig.41b) show some chipping, probably from the rim. This occured independent of temperature, but not on all specimen locations, being probably inhibited by improved surface smoothness.

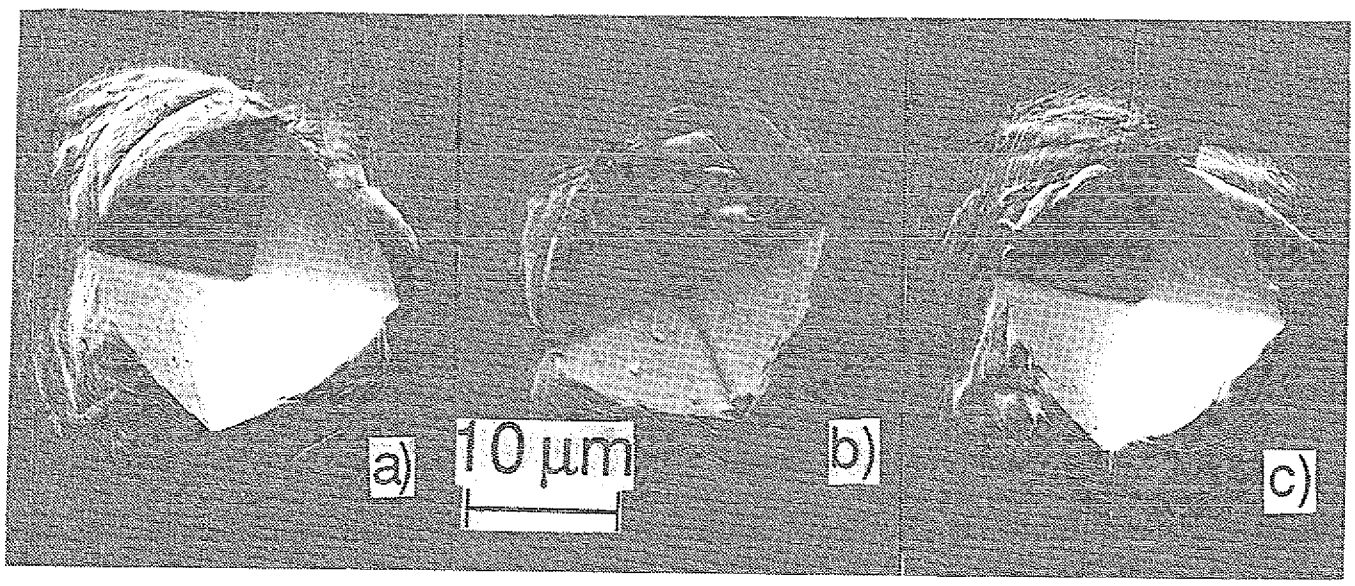

Fig.41: SEM (5 kV) pictures after indentation fatigue (a,b) and indentation creep (c) on MANET II martensitic stainless steel at 80°C with 44.1° indenter at maximum load of 0.5 N, cf. fig.40.

5.7. Hardness measurements on stressed specimens

It was also tried to investigate the effect of superposing an external tensile stress to the inherent compressive stress under hardness testing. This was achieved by convex bending of foil specimens of thickness d on a radius r which was determined by:

$$r = d / 2\epsilon \qquad (23)$$

where the strain ϵ on the tensile side was about 0.4%, i.e. the imposed tensile stress was about the conventional $\sigma_{0.2}$ yield stress. Figure 42 shows that in MANET II the measured hardness was reduced by bending, but only at temperatures from about -130° to -10°C, while at higher temperatures the difference disappeared. A reduction of hardness by up to 12% due to tensile stresses has also been observed in ref.[98], while in thin films [75] no significant effect of stress (tensile or compressive) on hardness was found.

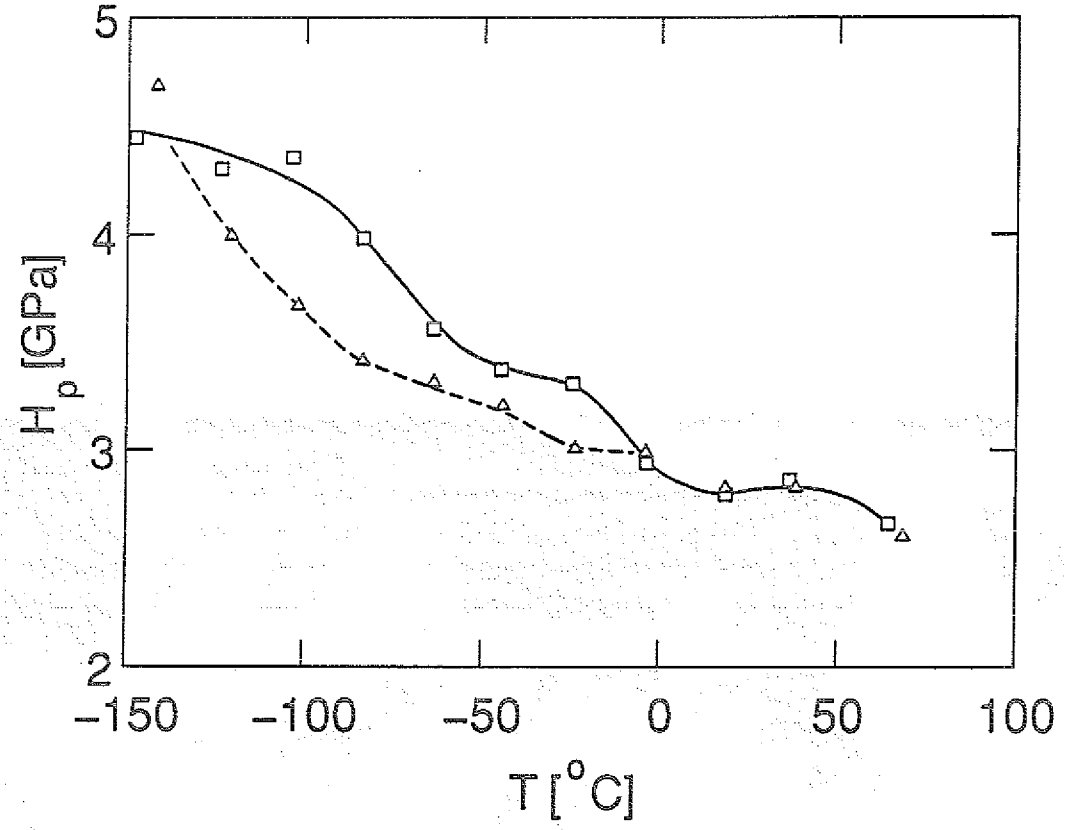

Fig.42: Hardness testing on flat (□) and on bent (△) MANET II specimens with a α=44.5° indenter. The specimen thickness was 100 μm and the bending radius was 12 mm, corresponding to a tensile strain of 0.4% on the tensile surface.

6. Discussion

6.1. Relation of ISE to other mechanical properties

The phenomenological description of ISE by equation (8) to some degree resembles that of the Hall-Petch relation between strength σ and grain diameter s:

$$\sigma = \sigma_0 + k/\sqrt{s} \qquad (24)$$

with $k=k_0 \cdot \mu \cdot \sqrt{b}/\pi$ (μ=shear modulus, b=Burger vector) and average values of $k_0 \approx 1/3$ for fcc and ≈ 1 for bcc metals, cf. ref.[99]. Recent investigations show that with few exceptions [100] relation (24) holds only down to some minimum grain size of about 1 μm in nickel [101] and 12 μm in iron [102]. Also investigations on nanocrystalline material show strongly reduced [103] or even negative [104] k-values at very small grain sizes. This change of k has also been tentatively explained by a geometrical restriction of the operation of dislocation sources in very small grains [105]. An increased hardness and strength below thicknesses around 1 μm of Al-films on Si-substrates has been attributed to geometrical effects on dislocation behaviour [75].

6.2. Ductile to brittle transition of martensitic steel

Similar to tensile properties [51,52], the present microhardness data do not show a sharp transition which could be directly associated with DBTT. Nevertheless a temperature shift can be assigned to the hardness curves after implantation or irradiation. In figure 18 the temperature corresponding to H_p=3.57 GPa, i.e. the value corresponding to the DBTT ≈-25°C from CVN measurements of unirradiated material [36], was plotted as a function of displacement dose. At equal displacement dose the temperature shifts are significantly larger for the implanted specimens. In previous proton irradiations of 12%Cr-martensitic steels to very small doses no irradiation effect was found in disk-bend tests [106]. In figure 43 the results from the present hardness measurements on irradiated specimens are compared to results of Charpy-V-notch tests on reactor irradiated 12%Cr martensitic steels. As the irradiation induced shift in DBTT diminishes for irradiation temperatures above about 400°C and almost vanishes above 475°C [36,107,108], only data from irradiations below 400°C are included. Obviously the present data of the room temperature irradiated specimens (--) are above the trend of CVN measurements at 300°C on MANET I (+,[36]) and low dose measurements on two other 12Cr-1MoVW martensitic steels [108,109], irradiated at 300°C (x,△). On the other hand the present value after 520°C proton irradiation (-·-) is slightly below. Recent results indicate that DBTT shift may also decrease at temperatures below 400°C [110,111], possibly showing a slower increase but a higher saturation value of △DBTT at the lower temperatures [111]. More investigations in this temperature regime are needed before a more detailled comparison is possible.

The much larger temperature shift observed at equal displacement dose in helium implanted specimens (fig.18) is in agreement with results on Ni-doped specimens irradiated in HFIR to produce helium by transmutation [112], while in ref.[63] no significant difference between DBTT shifts of Ni-doped (to increase helium production by transmutation) and undoped specimens was found. One problem in this respect is that Ni-doping by itself changes mechanical and aging properties of these steels. For compositional effects on DBTT, compare ref.[63]. Therefore additional investigations are also needed to compare these two methods of helium production - implantation versus Ni-doping - and their usability to assess the effect of transmutation helium on DBTT of martensitic steels.

The annealing results clearly indicate that the DBTT shifts after high temperature irradiation or implantation are quite differentz from those observed after annealing of specimens irradiated ate lower temperatures.

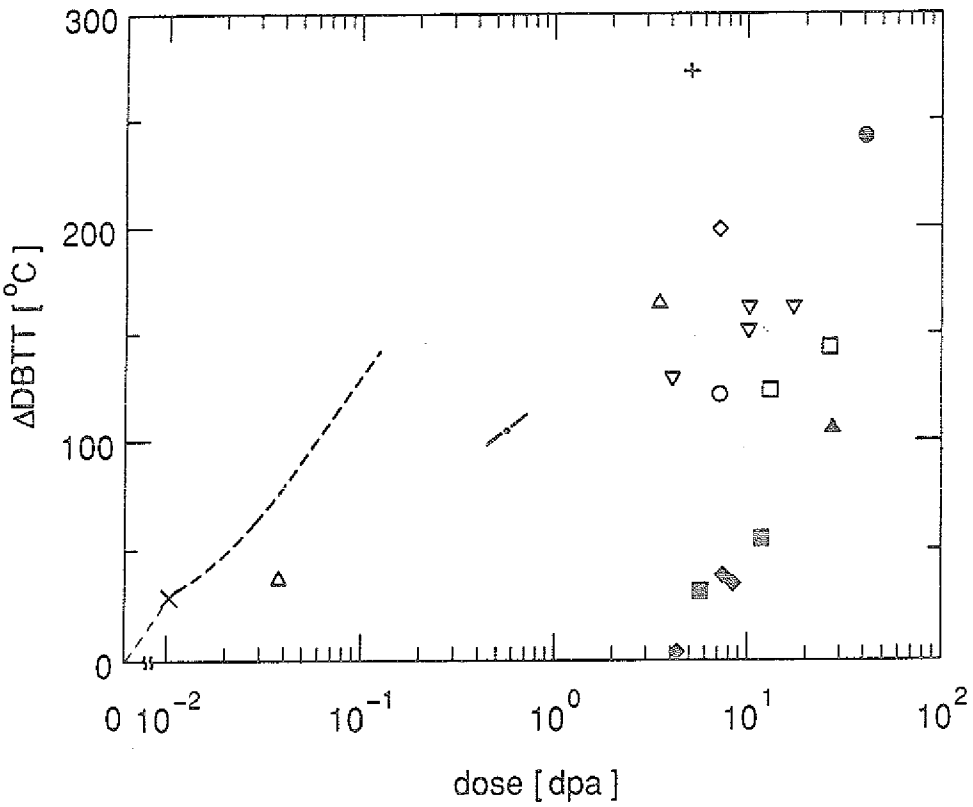

Fig.43: Comparison of the temperature shift of hardness at 3.57 GPa of room temperature irradiated specimens (--,fig.18) and after 520°C irradiation (-•-) to DBTT shifts in 12% Cr steels after reactor irradiation measured by CVN on MANET I at 300°C (+) [36]; on HT-9 at 55°C (▀) [113] and 390°C (_) [111]; on 12Cr-1MoVW at 50°C ( ), at 300°C (△) [108], (△) [110], at 330°C ( ) [52], at 365°C (▽) [114,115], and 400°C (o) [115], (o) [110]; and on JFMS-5 at 300°C (x) [109]. Full symbols indicate irradiation in HFIR, others in fast reactors.

7. Summary

The instrumented hardness testing device at variable temperature was used for variety of investigations, giving among others the following results:

1) Al, Cu, 316L and to some degree 1.4914 show indentation size effects which can be ascribed to an extra hardening contribution from the rim of the indentation. The hard materials W and Si show no identation size effect.

2) The ratios H_0/H_∞ of the hardness of the rim (H_0) to that of the bulk (H_∞) show no systematic dependence on indentation angle and decrease with increasing hardness of the material from ≈2.4 (Al) to 1 (Si,W).

3) The widths of the effective rim area show no systematic dependence on indentation angle or material and range from about 1 to 3 μm.

4) From hardness measurements with different indentation angles yield strengths were extrapolated and strain-hardening coefficients derived.

5) From unloading after indentation, Young's modulus is derived in reasonable agreement with literatur data.

6) Microhardness of DIN1.4914 martensitic stainless steel is increased by irradiation and by helium implantation.

7) The enhanced hardness can be associated with a shift of DBTT.

8) At equal displacement dose the He-implanted specimens show significantly larger shifts than specimens irradiated without implantation.

9) Ion irradiation changes the hardness of phosphide containing brazes used for joining stainless steels.

10) Thin silica layers on silicon-carbide were identified by their Young's modulus derived from hardness measurements.

References

[1] J.P.Pethica, R.Hutchings and W.C.Oliver, Philos.Mag.A 48 (1983) 593

[2] J.L.Loubet, J.M.Georges, J.M.Marchesini and G.Meille, J. Tribology 106 (1984) 43

[3] P.E.Wierenga and A.J.J.Frenken, J.Appl.Phys. 55 (1984) 4244

[4] D.Newey, M.A.Wilkins and H.M.Pollock, J. Phys. E15 (1982) 119

[5] D.Tabor, Proc.Royal Soc. A 192 (1948) 247 and "Hardness of Metals", Clarendon 1951

[6] C.Rubenstein, Trans ASME 48 (1981) 796

[7] D.Tabor, ASTM-STP 889 (1986) 129

[8] M.F.Doerner and W.D.Nix, J.Mater.Res. 1 (1986) 601

[9] H.Bückle in The Science of Hardness Testing and its Research Applications (J.H.Westbrook and H.Conrad, Eds.), ASM, Metals Park Ohio, USA (1973) p.453

[10] H.Bückle, Metall.Reviews 4 (1959) 49

[11] L.E.Samuels, ASTM-STP 889 (1986) 5

[12] J.L.Loubet, J.M.Georges and G.Meille, in Microindentation Techniques in Materials Science and Engineering, ASTM-STP 889, (Eds.P.J.Blau and B.R.Lawn), 1986, pp72-89

[13] B.R.Lawn and V.R.Howes, J.Mater.Sci. 16 (1981) 2745

[14] G.M.Pharr and R.F.Cook, J.Mater.Res. 5 (1990) 847

[15] I.N.Sneddon, Int.J.Engng.Sci. 3 (1965) 47

[16] I.E.Samuels and T.O.Mulhearn, Journal of the Mechanics and Physics of Solids, 5 (1957) 125

[17] H.Shi and M.Atkinson, J.Mater.Sci. 25 (1990) 2111

[18] M.Atkinson, Int.J.Mech.Sci. 33 (1991) 843

[19] K.Yasuda, K.Shinohara, M.Yamada, M.Kutsuwada and C.Kinoshita, J.Nucl.Mater. 187 (1992) 109

[20] M.Atkinson and H.Shi, Mater.Sci.Technol. 5 (1989) 613

[21] D.Lebouvier, P.Gilormini and E.Felder, J.Phys.D:Appl.Phys. 18 (1985) 199

[22] P.M.Sargent, in: Microindentation Techniques in Materials Science and Engineering, P.J.Blau and B.R.Lawn, eds., ASTM-STP 889 (1986) 160

[23] G.P.Upit and S.A.Varchenya in: The Science of Hardness Testing and its Research Applications, J.H.Westbrook and H.Conrad, eds., ASM, Metals Park Ohio, USA (1973) p.135

[24] O.Vingsbo, S.Hogmark, B.Jönsson and A.Ingemarsson, ASTM-STP 889 (1986) 257

[25] G.Farges and D.Degout, Thin Solid Films 181 (1989) 365

[26] B.W.Mott, Microindentaion Hardness Testing, Butterworth, London, 1957

[27] M.J.Makin and F.J.Minter, Acta Metall.8 (1960) 691

[28] G.J.Kraaij, KFA Jülich, Report Jül-Spez-94 (1980), ISSN 0343-7639

[29] K.Ehrlich, Kernforschungszentrum Karlsruhe, Primärbericht: Formulation of Initial Design Equations for Type 1.4914 Martensitic Steel, Report NET 84-038/T (1986)
[30] P.Marmy, Y.Ruan and M.Victoria, Report Paul Scherrer Institut, CH-5232 Villigen, PSI-Bericht Nr.37 (1989)
[31] American Inst. of Phys. Handbook, McGraw-Hill, USA (1957)
[32] K.Ehrlich and K.Anderko, J.Nucl.Mater. 124 (1984) 229
[33] G.E.Lucas, G.R.Odette, J.W.Sheckherd, P.McConnell and J.Perrin, ASTM-STP 888 (1986) 305
[34] W.R.Corwin and A.M.Hougland, ASTM-STP 888 (1986) 325
[35] R.L.Klueh and D.J.Alexander, J.Nucl.Mater. 191-194 (1992) 896
[36] C.Wassilew and K.Ehrlich, J.Nucl.Mater. 191-194 (1992) 850
[37] T.Kondo, D.G.Doran, K.Ehrlich and F.W.Wiffen, J.Nucl.Mater. 191-194 (1992) 100
[38] H.Kayano, H.Kurishita, A.Kimura, M.Narui, M.Yamazaki and Y.Suzuki, J.Nucl.Mater. 179-181 (1991) 425
[39] F.H.Huang, ASTM-STP 888 (1986) 290
[40] P.McConnell, J.W.Sheckherd, J.S.Perrin and R.A.Wullaert, ASTM-STP 888 (1986) 353
[41] A.Kohyama, K.Hamada and H.Matsui, J.Nucl.Mater. 179-181 (1991) 417
[42] K.K.Bae, K.Ehrlich and A.Möslang, J.Nucl.Mater. 191-194 (1992) 905
[43] A.Hasegawa and H.Shiraishi, J.Nucl.Mater. 191-194 (1992) 910
[44] M.Suzuki, M.Eto, K.Fukaya, Y.Nishiyama, T.Kodaira, T.Oku, M.Adachi, A.Umino, I.Takahashi, T.Misawa and Y.Hamaguchi, J.Nucl.Mater. 179-181 (1991) 441
[45] T.Misawa, K.Suzuki, M.Saito and Y.Hamaguchi, J.Nucl.Mater. 179-181 (1991) 421
[46] J.McNaney, G.E.Lucas and G.R.Odette, J.Nucl.Mater. 179-181 (1991) 429
[47] A.Okada, M.L.Hamilton and F.A.Garner, J.Nucl.Mater. 179-181 (1991) 445
[48] F.Abe, T.Noda, H.Araki, M.Okada, M.Narui and H.Kayano, J.Nucl.Mater. 150 (1987) 292
[49] T.Misawa, T.Adachi, M.Saito and Y.Hamaguchi, J.Nucl.Mater. 150 (1987) 194
[50] J.-M.Baik, J.Kameda and O.Buck, ASTM-STP 888 (1986) 92
[51] A.Kohyama, H.Matsui, K.Hamada and H.Simidzu, J.Nucl.Mater. 155-157 (1988) 896 and A.Kohyama,K.Hamada, K.Asakura and H.Matsui, ASTM-STP 1046 (1990) 404
[52] F.Abe, T.Noda, H.Araki, M.Narui and H.Kayano, J.Nucl.Mater. 166 (1989) 265
[53] D.Pachur and G.Sievers, ASTM-STP 570 (1975) 555
[54] G.R.Odette, P.M.Lombrozo and R.A.Wullaert, ASTM-STP 870 (1985) 840
[55] G.R.Odette, P.M.Lombrozo and R.A Wullaert, ASTM-STP 870 (1985) 840
[56] R.A.Wullaert, D.R.Ireland and A.S.Tetelman, ASTM-STP 484 (1970) 20

[57] N.M.Ghoniem and R.W.Conn, IAEA-TC-392/62, p.389
[58] J.F.Mancuso, J.A.Spitznagel, R.P.Shogan and J.R.Holland,
[59] K.Shinohara, G.e.Lucas and G.R.Odette, J.Nucl.Mater. 133&134 (1985) 326
[60] N.F.Panatayotou, J.Nucl.Mater. 108&109 (1982) 456
[61] H.Matzke, Key Engineering Mater. 56-57 (1991) 365
[62] D.J.Rowcliffe, Key Engineering Mater. 71 (19921) 1
[63] W.R.Corwin, J.M.Vitek and R.L.Klueh, J.Nucl.Mater. 149 (1987) 312
[64] P.Jung and V.Sciani, in Diffusion in Matals and Alloys (F.J.Kedves and D.L.Beke, Eds.), Trans Tech Publication, 1983, p.446
[65] P.Jung, J.Nucl.Mater. 117 (1983) 70
[66] Z.S.Basinski and J.W.Christian, Austr.J.Phys. 13 (1960) 299
[67] K.Kitajima, E.Kuramoto, Y.Aono and H.Abe in Mech.Prop.of bcc Metals (M. Meshii,Ed.) AIME 1982, p.111
[68] H.Kimura, H.Matsui and S.Takaki in Mech.Prop.of bcc Metals (M. Meshii,Ed.) AIME 1982 p.125
[69] Z.Zhu, P.Jung and H.Klein, J.Nucl.Mater., to be published
[70] U.Stamm and H.Schroeder, J.Nucl.Mater. 155-157 (1988) 1059
[71] L.Boulanger, P.Bellen, Y.Seruys, N.V.Doan and G.Martin, J.Nucl.Mater. 191-194 (1992) 473
[72] L.Boulanger, J.Chen, P.Jung and Y.Seruys, J.Nucl.Mater., to be published
[73] C.Brown and G.Linekar, UKAEA TRG-Memo-6571, 1974
[74] W.G.Wolfer and B.B.Glasgow, Acta Metall. 33 (1985) 1997
[75] M.F.Doerner, D.S.Gardner and W.D.Nix, J.Mater.Res. 1 (1986) 845
[76] A.K.Sinha and T.T.Sheng, Thin Solid Films 48 (1978) 117
[77] W.Pill-Kauffmann, Report KFA Jülich Jül-2436 (1991) ISSN 0366-0885
[78] H.Bangert and A.Wagendristel, J.Vac.Sci.Technol. A4 (1986) 2956
[79] H.Bangert and A.Wagendristel, Rev.Sci.Instrum. 6 (1985) 1568
[80] P.A.Engel and M.D.Derwin, in Microindentation Techniques in Materials Science and Engineering, ASTM-STP 889 (1986) 272
[81] H.M.Pollock, D.Maugis and M.Barquins, in Microindentation Techniques in Materials Science and Engineering, ASTM-STP 889 (1986) 47
[82] J.B.Pethica in: Ion Impl. to Metals, V. Ashworth, W.A.Grant and R.P.M.Procter, eds., Pergamon Press (1982), p.147
[83] D.Tabor, J.Inst.Metals 79 (1951) 1
[84] J.R.Cahoon, W.H.Broughton and A.R.Kutzak, Met.Trans. 2 (1971) 1979
[85] H.Bangert, A.Wagendristel and H.G.Guenther, Thin Film Technol. II (1986) 134
[86] J.D.J.Ross, H.M.Pollock, J.C.Pivin and J.Takadoum, Thin Sol.Films 148 (1987) 171

[87] J.E.Bird, A.K.Mukherjee and J.E.Dorn, Int.Conf.on Quant.Rel.between Prop.and Microstr., Haifa 1969, Israel Univ.Press, p.255
[88] E.N.da C.Andrade, Proc.Royal.Soc.A 84 (1910) 1
[89] P.G.McVetty, Mech.Eng. 56 (1934) 149
[90] K.E.Amin, A.K.Mukherjee and J.E.Dorn, J.Mech.Phys.Sol. 8 (1970) 413
[91] O.D.Sherby, T.A.Trozera and J.E.Dorn, Proc.ASTM 56 (1956) 784
[92] J.Weertman, J.Mech.Phys.Sol. 4 (1956) 230
[93] A.G.Atkins, A.Silverio and D.Tabor,J.Inst.Met. 94 (1966) 369 and A.G.Atkins in: The Sci.of Hardness Test.and its Res.Appl., J.H.Westbrook, A.Conrad, eds., ASM 1971, p.223
[94] J.L.Lytton, L.A.Shepard and J.E.Dorn, Trans.Met.Soc.AIME 212 (1958) 220
[95] D.A.J.Vaughan, F.Guiu and M.R.Dalmau, J.Mater.Sci.Lett. 6 (1987) 689
[96] M.Reece and F.Guiu, J.Am.Ceram.Soc. 73 (1990) 1004
[97] J.C.M.Li and S.N.G.Chu, Scripa Metall. 13 (1979) 1021
[98] T.R.Simes, s.G.Mellor and D.A.Hills, J.Strain Anal. 19 (1984) 135
[99] P.M.Kelly, J.Austr.Inst.Met. 16 (1971) 104
[100] J.D.Embury, A.S.Keh and R.M.Fisher, Trans.AIME 236 (1966) 1252
[101] A.A.W.Thompson, Acta Met. 23 (1975) 1337
[102] E.Anderson, D.L.W.King and J.Spreadborough, Trans AIME 242 (1968) 115
[103] G.W.Nieman, J.R.Weertman and R.W.Siegel, Scripta Metall. 23 (1989) 2013
[104]A.H.Chokshi, A.Rosen, J.Karch and H.Gleiter, Scripta Metall. 23 (1989) 1679
[105] E.P.Abrahamson, Surfaces and Interfaces II, Syracuse Univ.Press, Syracuse, USA (1968) p.262
[106] Y.Hamaguchi, H.Kuwano, T.Misawa, R.Miura and T.Yamada, J.Nucl.Mater. 141-143 (1986) 781
[107] W.Vandermeulen, Fusion Technol. 2 (1986) 1025
[108] J.M.Vitek, W.R.Corwin, R.L.Klueh and J.R.Hawthorne, J.Nucl.Mater. 141-143 (1986) 948
[109] H.Kayano, H.Kurishita, A.Kimura, M.Narui, M.Yamazaki and Y.Suzuki, J.Nucl.Mater. 179-181 (1991) 425
[110] R.L.Klueh and D.J.Alexander, J.Nucl.Mater. 179-181 (1991) 733
[111] D.S.Gelles, J.Nucl.Mater. 149 (1987) 192
[112] R.L.Klueh and P.J.Maziasz, ASTM-STP 1046 (1989) 246
[113] W.-L.Hu and D.S.Gelles, ASTM-STP 1046 (1990) 453
[114] R.L.Klueh and D.J.Alexander, J.Nucl.Mater. 191-194 (1992) 896
[115] R.L.Klueh and D.J.Alexander ASTM-STP 1125 (1992) 1256
[116] R.L.Klueh, J.M.Vitek, W.R.Corwin, R.L.Klueh and D.J.Alexander, J.Nucl.Mater. 155-157 (1988) 973

FORSCHUNGSZENTRUM JÜLICH GmbH

KFA

Jül-2822
Oktober 1993
ISSN 0944-2952